

1-1-2013

# Imaging the Electro-Kinetic Response of Biological Tissues with Optical Coherence Tomography

Valentin Demidov  
*Ryerson University*

Follow this and additional works at: <http://digitalcommons.ryerson.ca/dissertations>

 Part of the [Medical Biophysics Commons](#)

---

## Recommended Citation

Demidov, Valentin, "Imaging the Electro-Kinetic Response of Biological Tissues with Optical Coherence Tomography" (2013). *Theses and dissertations*. Paper 2067.

This Thesis is brought to you for free and open access by Digital Commons @ Ryerson. It has been accepted for inclusion in Theses and dissertations by an authorized administrator of Digital Commons @ Ryerson. For more information, please contact [bcameron@ryerson.ca](mailto:bcameron@ryerson.ca).

**IMAGING THE ELECTRO-KINETIC  
RESPONSE OF BIOLOGICAL TISSUES  
WITH OPTICAL COHERENCE TOMOGRAPHY**

by

Valentin Demidov

B.Sc., Saratov State University, Saratov, Russia 2000

A thesis

presented to Ryerson University in

partial fulfillment of the

requirements for the degree of

Master of Science

in the Program of

Biomedical Physics

Toronto, Ontario, Canada, 2013

© Valentin Demidov 2013

## **Author's Declaration**

I hereby declare that I am the sole author of this thesis. This is a true copy of the thesis, including any required final revisions, as accepted by my examiners.

I authorize Ryerson University to lend this thesis to other institutions or individuals for the purpose of scholarly research.

I further authorize Ryerson University to reproduce this thesis by photocopying or by other means, in total or in part, at the request of other institutions or individuals for the purpose of scholarly research.

I understand that my thesis may be made electronically available to the public.

---

VALENTIN DEMIDOV

# **Imaging the Electro-Kinetic Response of Biological Tissues with Optical Coherence Tomography**

Valentin Demidov

M.Sc., Biomedical Physics, Ryerson University, 2013

## **Abstract**

This thesis reports on developing a novel approach to imaging the electro-kinetic response of biological tissues with optical coherence tomography (OCT). The changes of backscattered OCT signal from tissues were investigated with a low frequency AC electric field being applied to the tissues. Advanced processing algorithms were developed to analyze the amplitude and phase changes of OCT signal. Two-dimensional electrically induced optical changes (EIOC) amplitude and phase images related to the electro-kinetic response of soft tissues were obtained with depth resolution and compared with structural OCT images. The procedure for removing the background noise from EIOC images was introduced.

## **Acknowledgements**

I would like to warmly acknowledge the continuous encouragement, timely suggestions and inspired guidance offered by my supervisors Dr. Vladislav Toronov and Dr. Yuan Xu, Associate Professors of Biomedical Physics Department.

I am grateful to Dr. Victor Yang, Associate Professor of Department of Electrical and Computer Engineering, for permitting me to make use of the facilities available in his laboratory to carry out the project successfully.

Special thanks to Professor Alex Vitkin at University of Toronto for scientific assessment of the potential of this project, valuable comments and positive attitude. His enthusiasm for my topic and tremendous expertise are very much appreciated.

Last but not the least I express my sincere thanks to my colleagues Krzysztof Wawrzyn, Barry Vuong and Carry Sun who have patiently extended all sorts of help for accomplishing this undertaking.

# Table of Contents

<b>1. INTRODUCTION</b> .....	1
1.1 The effect of electric field on biological tissues .....	1
1.2 Electric properties of biological tissues .....	3
1.3 Electro-kinetic phenomena.....	6
1.4 Imaging the electro-kinetic phenomena .....	9
1.5 Optical coherence tomography.....	15
1.6 Thesis objectives and outline .....	22
References .....	23
<b>2. Imaging the electro-kinetic response of biological tissues by using the amplitude of optical coherence tomography</b> .....	30
Abstract .....	31
2.1 Introduction .....	32
2.2 Experimental Setup .....	33
2.3 Results .....	34
2.3.1 1D-Mode .....	34
2.3.2 2D-Mode .....	36
2.4 Discussion .....	38
2.5 Conclusion.....	39
References .....	40
<b>3. Imaging the electro-kinetic response of biological tissues by using the phase of optical coherence tomography</b> .....	43
Abstract .....	44
3.1 Introduction .....	44
3.2 Experimental methods.....	46
3.2.1 Specimen Preparation .....	46
3.2.2 OCT Instrumentation .....	47
3.2.3 Experiment Protocol (Data Acquisition) .....	48

3.3	Development of phase imaging algorithm .....	48
3.4	Results .....	56
3.4	Discussion .....	59
3.4	Conclusion.....	62
3.4	Acknowledgements .....	63
	References .....	63
<b>4.</b>	<b>SUMMARY OF RESULTS, CONCLUSIONS AND FUTURE WORK .....</b>	<b>67</b>
4.1	Summary of results and conclusions.....	67
4.2	Future work .....	69
	References .....	71

## Table of Figures

Figure 1.1 Schematic of fixed charge density in biological tissue. ....	7
Figure 1.2 Schematic of double layer in a liquid at contact with a positively-charged solid surface. ....	7
Figure 1.3 Schematic of interfacial double layer [21]. ....	8
Figure 1.4 Schematic of the experimental setup in [28], used to detect the electric-field induced mechanical changes (EIMC) in bulk tissues including deformation and strain. ....	10
Figure 1.5 Detected ultrasound signals. Aa and Ab denote the peak-to-peak value of the signal within a small window after and before electric field application to the sample [28]. Echo amplitudes were represented by Aa and Ab, while phases were represented by the arrival times of the peaks in each individual window. ....	10
Figure 1.6 Peak-to-peak amplitude in 4 windows of echo signals from a pork heart tissue. Positive (in solid rectangle) and negative (in dashed rectangle) DC voltage were applied for 45 and 48 seconds, respectively. (a) signal amplitude changes; (b) signal phase changes [28]. ....	11
Figure 1.7 Schematic of streaming potential mechanism in cartilage. ....	12
Figure 1.8 Schematic of differential phase optical coherence reflectometer. ....	12
Figure 1.10 Schematic of stimulating waveform (top) and trigger sequence for data acquisition (bottom) [32]. ....	13
Figure 1.9 Schematic of the physically deformed cartilage in response to stimulation. ....	13
Figure 1.11 Surface displacement amplitude within cartilage generated by 1, 0.5 and 0.2Hz excitation. ....	14
Figure 1.12 Schematic presentation of swept-source optical coherence tomography. ....	17
Figure 1.13 Recorded intensity $I(w)$ for the number of $w$ frequencies. ....	19
Figure 1.14 Amplitude of the OCT signal backscattered from the biological tissue sample. ....	20
Figure 1.15 Phase of the OCT signal backscattered from the biological tissue sample. ....	21
Figure 2.1 Diagram of the experimental setup. ....	33
Figure 2.2 (a) The time course of a typical OCT signal acquired on a sample before, during (inside the solid square), and after the AC voltage application. (b) same time course after de-trending. (c) Fourier spectrum of 3 portions of the signal. ....	35
Figure 2.3 Dependence of average EIOC amplitude on: (a) the amplitude and (b) the frequency of the applied voltage. ....	36
Figure 2.4 Illustration of the EIOC image processing algorithm. ....	37

Figure 2.5 (a) Original OCT image; (b) Un-normalized OCT-based EIOC image; (c) EIOC background image during electric field application; (d) OCT-based EIOC image normalized by the EIOC background image during electric field application.....	38
Figure 3.1 Schematic presentation of the experimental setup. ....	47
Figure 3.2 Timing diagram for data acquisition. ....	49
Figure 3.3 Diagram of the 2D phase image processing algorithm, showing the analysis path from raw phase image (bottom right) to background and EIOC images (middle right). The last step (shown in the Figure 3.10(h) below) was pixel-wise division of EIOC image by the background image. ....	49
Figure 3.4 Typical phase temporal profiles for all depths of one A-line with grey scale bars in radians: (a) unwrapped phase (step 2 of the algorithm); (b) angular de-trended phase (step 4 of the algorithm); (c) temporal de-trended phase (step 6 of the algorithm). ...	51
Figure 3.5 Unwrapped phase curves before application of electric field to the sample in B-mode: a) single line, $t = 38$ s; b) all the lines, $t = 1 - 110$ s.....	52
Figure 3.6 The different range for smoothing the phase curves in angular de-trending procedure and corresponding 2D phase images: (a) 5 nearest points; (b) 21 nearest points; (c) 45 nearest points. Phase images were obtained after averaging 110 angular de-trended phase frames before AC application. Gray bars on the right of each image indicate the resulting difference between unwrapped and smoothed curves in radians. ....	53
Figure 3.7 (a) The time course of a typical OCT signal phase before, during (inside the solid square), and after the AC application. (b) The de-trended signal. (c) FFT transforms of signal portions before, during and after AC application. Peak in the spectra marked “measured frequency” corresponds to the same frequency of the applied electric field (0.1 Hz).....	54
Figure 3.8 The averaged (110 frames) amplitude <sup>10</sup> (a) and phase (b) OCT images before AC application with gray bars in log scale for amplitude and radians for phase. ....	56
Figure 3.9 <i>1<sup>st</sup> row</i> : Averaged phase images before (a), during (b) and after (c) AC application; <i>2<sup>nd</sup> row</i> : background phase images before (d), during (e) and after (f) AC application. <i>3<sup>rd</sup> row</i> : normalized averaged phase images before (g), during (h) and after (i) AC application. ....	57
Figure 3.10 <i>1<sup>st</sup> row</i> : EIOC phase images before (a), during (b) and after (c) AC application; <i>2<sup>nd</sup> row</i> : background phase images before (d), during (e) and after (f) AC application. <i>3<sup>rd</sup> row</i> : normalized EIOC phase images before (g), during (h) and after (i) AC application. Note that before and after AC application the resulting images (g) and (i) carry no information due to absence of electric current in the sample while (h) clearly demonstrates the difference during AC application. ....	58

Figure 3.11 (a) normalized EIOC amplitude image<sup>11</sup>; (b) normalized EIOC phase image; (c) their cross-correlation image. .... 60

# 1. INTRODUCTION

## 1.1 The effect of electric field on biological tissues

Electric field effects on biological tissues are of long-standing scientific interest with respect to sensory systems, medical applications, possible human health hazards, and food industry. In medical applications these are mainly electroporation for drug delivery and tissue ablation as local anticancer treatment [1], clinical electrocardiogram [2] and electroencephalogram [3] diagnoses, soft tissue wounds repair [4], and physiotherapy [5]. The success in these applications is highly dependent on parameters such as frequency and voltage of the applied field, tissue electrical properties and spatial relations in placement of electrodes that are used to establish a penetrating electric field in target tissue.

Biological tissue is characteristically a non-uniform segmented conducting dielectric, consisting of ~60% of water by weight, of which ~33% is intracellular and ~27% is extracellular [6]. In both the intracellular and extracellular compartments body fluids are highly electrolytic. These two compartments are separated by a relatively impermeable, highly resistive plasma membrane. When external electric field is applied to tissue, current conduction is carried by mobile ions in the tissue fluid. As the carriers for electrical current in metal electrodes are electrons, the current carriers change from electrons to ions when in contact with the tissue through electrochemical reactions [7].

At low frequencies of the applied electric field current becomes distributed. The electric field strength becomes nearly uniform throughout any plane that is perpendicular to the current path in tissue [8]. As a result, the electrical current density distribution depends on the relative electrical conductivity of different tissues and the current frequency. As was shown

experimentally with current distribution in the hind limb of anesthetized hogs in [8], the major arteries and nerves in tissues experienced the largest current density because of their higher conductivity. It was also observed that muscle tissues carried the majority of the current due to their predominant volumetric proportions.

At a microscopic scale, low-frequency electric field distribution within the tissue is determined by the shape, density, orientation, and size of cells. Low-frequency electrical current is mostly shielded from cytoplasmic fluid because the cell membrane functions as an ionic-transport barrier. The presence of cells reduces the space available for ionic current and therefore makes tissues less conductive. With increasing cell size in various tissues, the volume fraction of the cell occupied by the membrane is proportionately decreasing [9]. Consequently, membrane's impact on a cell's electrical properties decreases. For muscle tissues, resistivity measured perpendicular to the long axis of the muscle cells is more than that measured parallel to the axis. Fluids density in various types of tissue also affects resistivity. For epidermis where the free-water content is lower the resistivity is higher than for other biological tissues.

The distribution of higher frequencies current of radiofrequency and microwave ranges through the tissue depends on other parameters. Electric field pulses of duration in microseconds to milliseconds cause a temporary loss of the cell membranes permeability, thus leading to ion leakage, escape of metabolites, and increased uptake by cells of molecular probes, drugs, and DNA. A generally accepted term describing this phenomenon is "electroporation" [10]. At even higher electric field frequencies the membrane becomes not sealed; it readily permits passage of current into the cytoplasm, biochemical arrest occurs, and the permeabilized cell becomes necrotic.

## 1.2 Electric properties of biological tissues

Biological tissue can be broadly characterized as a conductive dielectric which electrical properties can be separated into two categories: conducting and insulating [11]. In a conductor, the electric charges move freely in response to the application of an electric field, whereas in an insulator (dielectric), the charges are fixed and not free to move. If a conductor is placed in an electric field, charges will move within the conductor until the interior field is zero. In the case of an insulator net migration of charge does not occur as no free charges exist.

In polar materials the positive and negative charge centers in the molecules do not coincide. An electric dipole moment,  $p$ , is said to exist [11]. An applied field,  $E_0$ , tends to orient the dipoles and produces a field  $E_p$  inside the dielectric, which opposes the applied field. This process is called polarization. Most materials including biological tissue contain a combination of relatively free charges and orientable dipoles so that the electric field is reduced relatively to its free-space value. The net field  $E$  inside the tissue is then

$$E = E_0 - E_p \quad (1)$$

The net field  $E$  is lowered by a significant amount relative to the applied field if the material is an insulator and is essentially zero for a good conductor. This reduction is characterized by a factor  $e_r$ , which is called the relative permittivity or dielectric constant:

$$E = \frac{E_0}{e_r} \quad (2)$$

In practice, most materials, including biological tissue, actually display some characteristics of both insulators and conductors because they contain dipoles and charges that can move, but in a restricted manner. Charges may become trapped at interfaces for materials that are heterogeneous in structure. As positive and negative ions move in opposite directions under the

applied field, internal charge separations can then result within the material, producing an effective internal polarization that acts like a very large dipole.

On a macroscopic level, tissue can be described as a material having permittivity  $\epsilon$ , and conductivity  $\delta$ . The permittivity characterizes the material's ability to trap or store charge or to rotate molecular dipoles, whereas the conductivity describes its ability to transport charge [12]. The energy  $u$  stored per unit volume in a material is

$$u = \frac{\epsilon E^2}{2} \quad (3)$$

and the power  $p$  dissipated per unit volume is

$$p = \frac{\delta E^2}{2} \quad (4)$$

In physical terms, conductivity of a tissue is a measure of the ability of its charge to be transported throughout its volume by an applied electric field. Similarly, its permittivity is a measure of the ability of its dipoles to rotate or its charge to be stored by an applied external field [11]. Note that if the permittivity and conductivity of the material are constant, the displacement current will increase with frequency whereas the conduction current does not change. At low frequencies (<100Hz), the tissue will behave like a conductor, but capacitive effects (heating) will become more important at higher frequencies. However, for most tissues these properties are not constant, but vary with the frequency of the applied signal [13].

The relative importance of the permittivity and conductivity in determining the electrical properties of the tissue can be compared by taking the ratio of the displacement and conduction currents:

$$\frac{I_d}{I_c} = \omega \frac{\epsilon}{\delta} \quad (5)$$

At low frequencies  $\omega$  this ratio is very low, even with the large increase in permittivity. Hence, at low frequencies, biological tissue is essentially conductive in nature [11].

The changes in electrical properties of biological tissue depend on many factors [16]. Tissue is a very inhomogeneous material. It contains cells of different sizes and functions. Tissue is distinctly anisotropic. Therefore, the orientation of the electrodes relative to the major axis of the tissue (e.g., longitudinal, transversal, or a combination of both) must be taken into account when measuring conductivity and permittivity. For example, muscles are composed of fibers that are very large individual cells and are aligned in the direction of the muscle contraction. As a consequence, electrical conduction along the length of the fiber is significantly higher than conduction between the fibers in the extracellular matrix because the extracellular matrix is less conductive than the cell [14,15].

Changes in tissue electrical properties reflect the changes in tissue physiology [17]. This principle has been used to identify or monitor the presence of various illnesses or conditions such as body fluid shift, blood flow, cardiac output, and muscular dystrophy by various impedance diagnostic techniques [18]. Tissue excision or death would result in significant changes in electrical properties. After the tissue has been excised the tissue metabolism decreases and tissue temperature falls. If the tissue is supported by temperature maintenance and perfusion systems, the tissue may be stabilized for a limited period of time in a living state *in vitro* (*ex vivo*). If the tissue is not supported irreversible changes will occur, followed by cell and tissue death [12]. If the blood flow is interrupted, metabolism continues but in an anaerobic way. Osmosis will cause cell swelling and tissue damage. As a consequence, the extracellular pathways narrow, which leads to an increase in the low frequency impedance. The time of occurrence of these phenomena is different for different tissues. Experimental results [16] show that during the first hour after the

tissue sample has been excised, the specific conductivity remains almost constant, although the change depends on the tissue type. Liver tissue shows changes after only 30 minutes from excision, brain tissue after one hour, and the muscle tissue two hours after excision. In all cases, the conductivity increases with time [16].

The electrical properties of tissue also depend on its temperature. The mobility of the ions that transport the current increases with the temperature as the viscosity of the extracellular fluid decreases. A general increase of about 2% per  $1\text{C}^{\circ}$  occurs in the conductivity of tissue [13] being subjected to a low-frequency electric field, up to a temperature of about  $40\text{C}^{\circ}$ . Above that point, the cell membrane begins to deteriorate and allows the cytosol to leak into the extracellular space.

### **1.3 Electro-kinetic phenomena**

In tissue, the cells are surrounded by an extracellular matrix, which can be extensive, as in the case of bone, or minimal, as in the case of epithelial tissue. In the extracellular matrix or on cell surfaces there are many molecules such as proteins and Glycosaminoglycan [19] that have net electric charges, which can be described by a fixed charge density (FCD) [20] schematically shown in Figure 1.1. Fixed charges cannot move around freely within the tissues when subjected to an electric field and therefore, do not contribute to conductivity. The electrical state of a charged surface is determined by the spatial distribution of ions around it [Figure 1.2]. Such a distribution of charges has traditionally been called the electrical double layer (EDL) [21]. The simplest picture of the EDL is a physical model in which one layer of the EDL is envisaged as a fixed charge or surface charge (so-called Stern layer), firmly bound to the particle or solid surface, while the other layer is distributed more or less diffusely within the solution in contact with the surface.

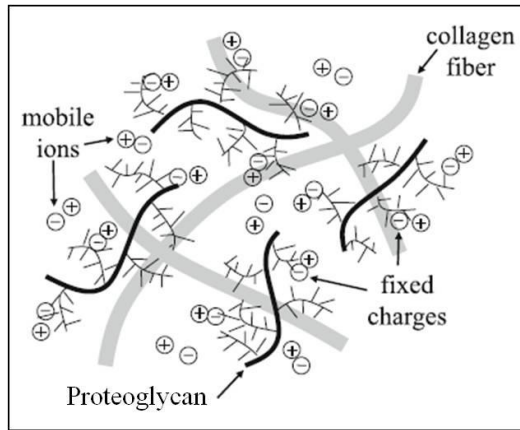


Figure 1.1 Schematic of fixed charge density in biological tissue.

This layer, called diffusive layer, contains an excess of counterions (ions opposite in sign to the fixed charge), and has a deficit of co-ions (ions of the same sign as the fixed charge). Surface charges create an electrostatic field that then affects the ions in the bulk of the solution.

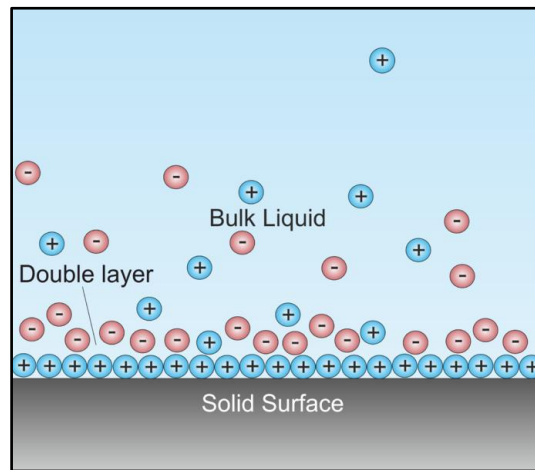


Figure 1.2 Schematic of double layer in a liquid at contact with a positively-charged solid surface.

The electrostatic field, in combination with the thermal motion of the ions, creates a counter charge, and thus screens the electric surface charge. The net electric charge in this screening diffuse layer is equal in magnitude to the net surface charge, but has the opposite polarity. As a result the complete structure is electrically neutral.

The diffuse layer, or at least part of it, can move under the influence of tangential stress caused by externally applied electric field. There is a conventionally introduced slipping plane that separates mobile fluid from fluid that remains attached to the surface [Figure 1.3]. Electric potential at this plane is called electro-kinetic potential or zeta potential. It is also denoted as  $\zeta$ -potential.

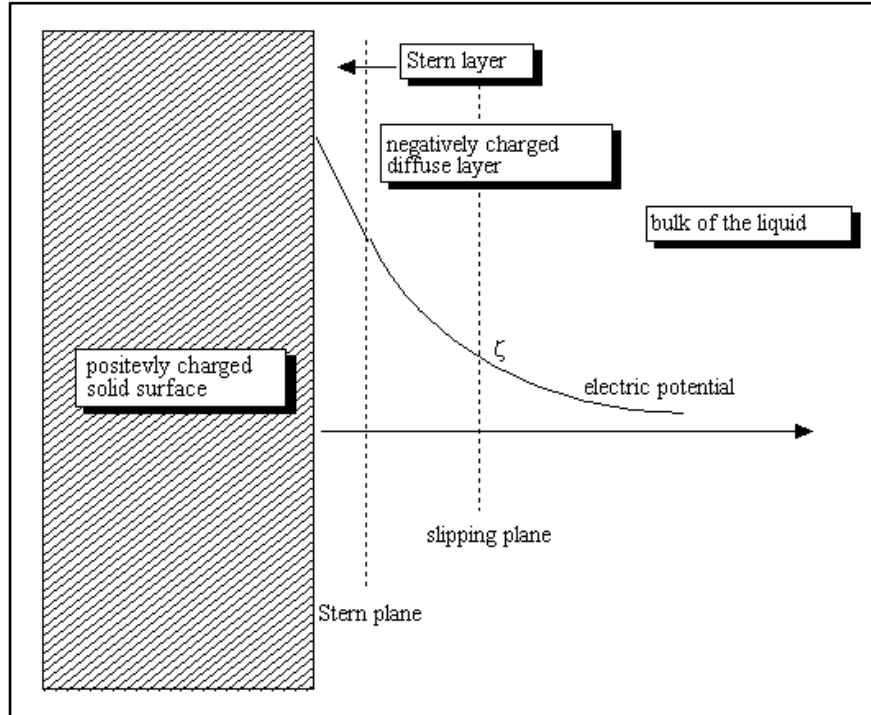


Figure 1.3 Schematic of interfacial double layer [21].

It is generally accepted [21] that  $\zeta$  is fully defined by the nature of the surface, its charge (often determined by pH), the electrolyte concentration in the solution, and the nature of the electrolyte and of the solvent. It can be said that for any interface with all these parameters fixed,  $\zeta$  is a well-defined property.

The movement of the diffuse layer causes interaction of mobile ions in interstitial fluid with fixed charges which lead to two generic phenomena, namely, the *electro-osmotic flow* and the *convective electric surface current* within the EDL. All electro-kinetic effects (electroosmosis,

electrophoresis, electroacoustic phenomena, streaming potential, etc.) originate from these two phenomena and are called collectively electro-kinetic phenomena (EKP). Electro-kinetic phenomenon like electro-osmotic flow, may be used for measuring zeta potential and consequently, defining electro-kinetic properties of tissue [22].

Electro-osmotic flow is the liquid flow along any section of the double layer under the action of the external field  $E$ . In Smoluchowski's theory [23], the electro-osmotic velocity is given by

$$v_{eo} = \frac{\varepsilon_{rs}\varepsilon_0\zeta}{\rho}E, \quad (6)$$

where  $\varepsilon_{rs}$  is the relative permittivity of the electrolyte solution,  $\varepsilon_0$  the electric permittivity of vacuum, and  $\rho$  is the dynamic viscosity of the liquid. From this, the electro-osmotic flow rate of liquid per current,  $Q_{eo,I}$  ( $\text{m}^3 \text{s}^{-1} \text{A}^{-1}$ ), can be determined as,

$$Q_{eo,I} = \frac{Q_{eo}}{I} = \frac{\varepsilon_{rs}\varepsilon_0\zeta}{\rho K_L}E, \quad (7)$$

with  $K_L$  being the bulk liquid conductivity (S/m) and  $I$  the electric current (A).

#### 1.4 Imaging the electro-kinetic phenomena

Different electric-field induced effects have been investigated by using optical microscopy in vitro in colloid, blood, and cell culture, to image changes in cellular shape [24], orientation [25] and migration [26].

Recently EKP have been imaged in various intact soft biological tissues ex-vivo [27-29]. In particular, ultrasound was employed to image the electric-field induced mechanical changes (EIMC) in bulk tissues including deformation and strain [28]. The electric current was applied to the porcine heart tissue sample through embedded at 5 cm distance electrodes (10-volt DC voltage or 0.025 Hz, 10-Volt AC) as schematically shown in Figure 1.4.

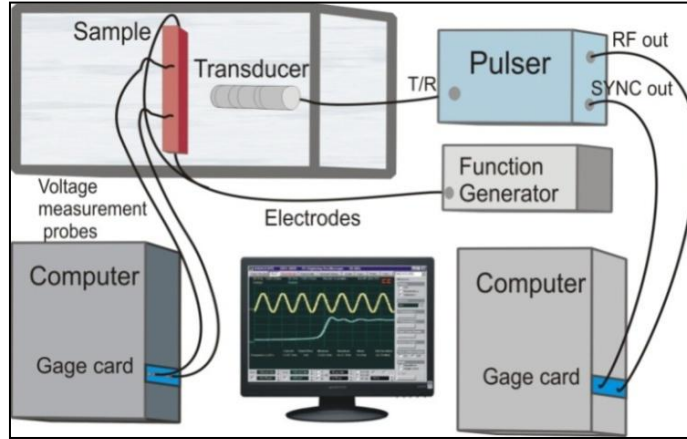


Figure 1.4 Schematic of the experimental setup in [28], used to detect the electric-field induced mechanical changes (EIMC) in bulk tissues including deformation and strain.

Ultrasound pulses were transmitted and received by a 10 MHz transducer, the echo signals (A-lines) were sampled at 200MS/s, averaged 2500 times and then analyzed. Some small windows were chosen in the ultrasound signals to analyze the amplitude and phase changes as shown in Figure 1.5. Echo amplitudes were represented by the peak values of the signals, while phases were represented by the arrival times of the peaks in each individual window.

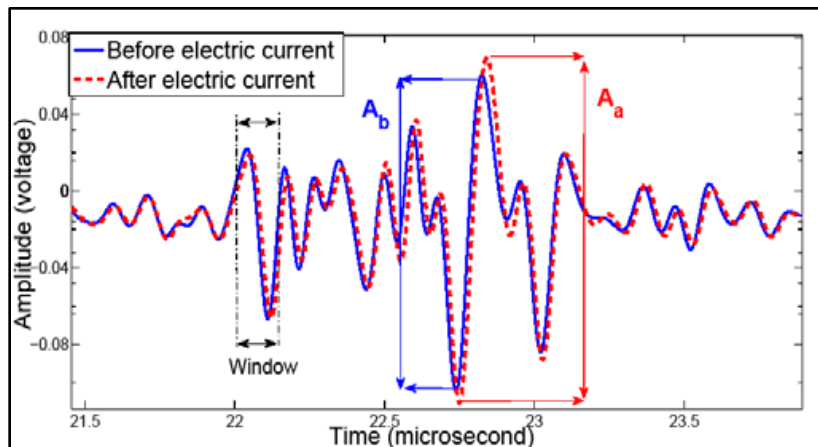


Figure 1.5 Detected ultrasound signals.  $A_a$  and  $A_b$  denote the peak-to-peak value of the signal within a small window after and before electric field application to the sample [28]. Echo amplitudes were represented by  $A_a$  and  $A_b$ , while phases were represented by the arrival times of the peaks in each individual window.

The results of the detected signals analysis demonstrated that when the polarity of the electric field was reversed, the sign of the change of the resulting amplitude also reversed [Figure 1.6(a)] but phase shifting did not [Figure 1.6(b)].

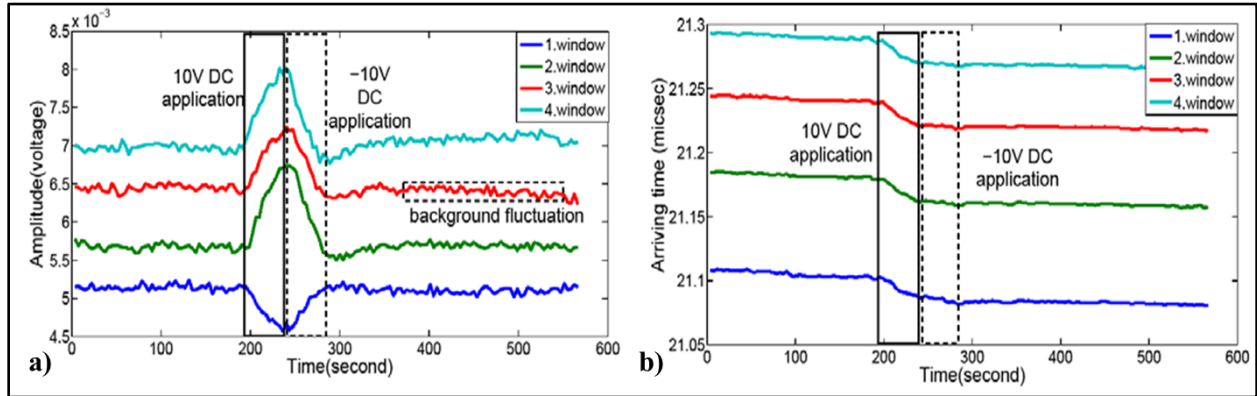


Figure 1.6 Peak-to-peak amplitude in 4 windows of echo signals from a pork heart tissue. Positive (in solid rectangle) and negative (in dashed rectangle) DC voltage were applied for 45 and 48 seconds, respectively. (a) signal amplitude changes; (b) signal phase changes [28].

It was concluded that the changes in amplitude and phase of the detected signals were associated with EIMC that were sensitive to the direction of the applied electric field in tissues and therefore related to EKP.

Frank and Grodzinsky measured the mechanical stress when the electric field was applied to the articular cartilage (a high FCD tissue) confined between two rigid plates [30, 31] as shown in Figure 1.7. The specimen was compressed by a porous electrode against an impermeable electrode in a cylindrically confined geometry. Upward fluid flow entrained mobile (+) counterions, having behind a small fraction of un-neutralized negative molecular charge groups. This slight charge separation generated a streaming potential field which produced conduction currents that were antiparallel to the fluid flow. The measured open circuit potential represented the balance between convective charge separation and the tendency of the conduction currents to maintain electro-neutrality, thereby ensuring zero net current.

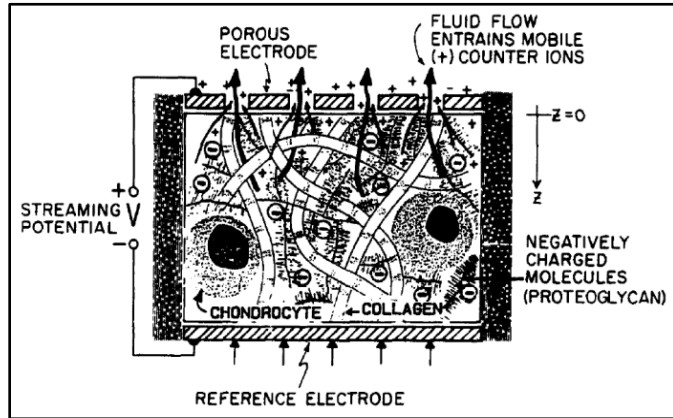


Figure 1.7 Schematic of streaming potential mechanism in cartilage.

By conducting these experiments Frank and Grodzynsky observed two additional electromechanical phenomena not previously seen in cartilage or other soft tissues: ‘streaming current’ and ‘current-generated stress’. Sinusoidal mechanical compression induced a sinusoidal streaming current density through cartilage disks when the Ag/AgCl electrodes that were used to compress the cartilage were shorted together externally. Conversely, a sinusoidal current density applied to the tissue generated a sinusoidal mechanical stress within the tissue.

Similarly, the surface displacements of cartilage tissue due to applied electric field were measured using optical reflectometry schematically shown in figure 1.8 [32].

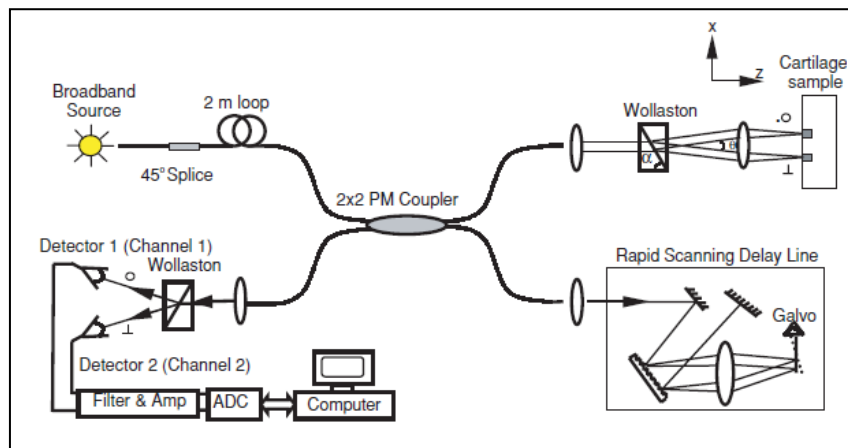


Figure 1.8 Schematic of differential phase optical coherence reflectometer.

Two platinum electrodes were used to stimulate cartilage electrically to induce electro-kinetic surface displacement [Figure 1.9]. In the sample path of reflectometer, the linearly polarized mutually orthogonal polarization fiber modes split in the Wollaston prism and the diverging beams from the prism were made parallel to each other and focused on the cartilage.

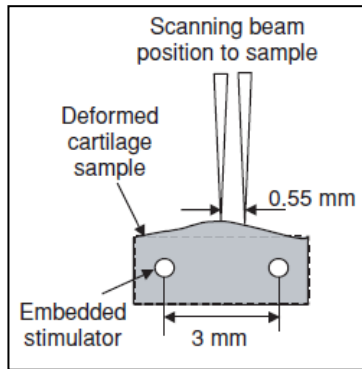


Figure 1.9 Schematic of the physically deformed cartilage in response to stimulation.

Backscattered light waves from the cartilage in both paths of the interferometer recombined and interfered at the 2x2 PM coupler. In the detection path, interfering light was split into two mutually orthogonal linearly polarized waves from each channel by a large angle Wollaston prism and detected by two photo-detectors. Figure

1.10 shows a timing diagram indicating how data were collected by the high-speed 12-bit analog/digital converter versus the stimulating waveform. A two-cycle sinusoidal waveform (SRS, DS 345) was applied to the platinum stimulation electrodes with peak amplitude voltages of 5 and 10 V at excitation frequencies of 0.2, 0.5 and 1.0 Hz. A square waveform (500 cycles) (Hewlett-Packard, 33120A) was applied to trigger and acquire the data. Acquisition of the fringe data was triggered at the rising edge of each square wave and 2048 points were recorded following each trigger event.

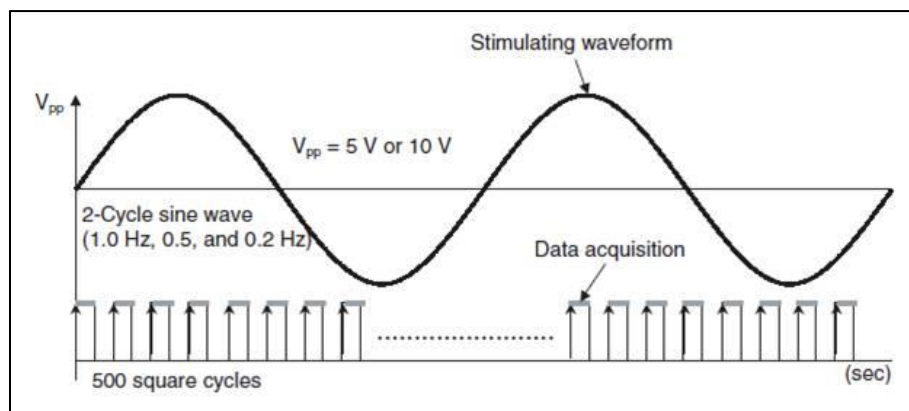


Figure 1.10 Schematic of stimulating waveform (top) and trigger sequence for data acquisition (bottom) [32].

The profiles induced by 5 and 10 V low-frequency electric field indicated that cartilage surface displacement increased with increased voltage and decreased with increased frequency of the applied electric field as shown in figure 1.11.

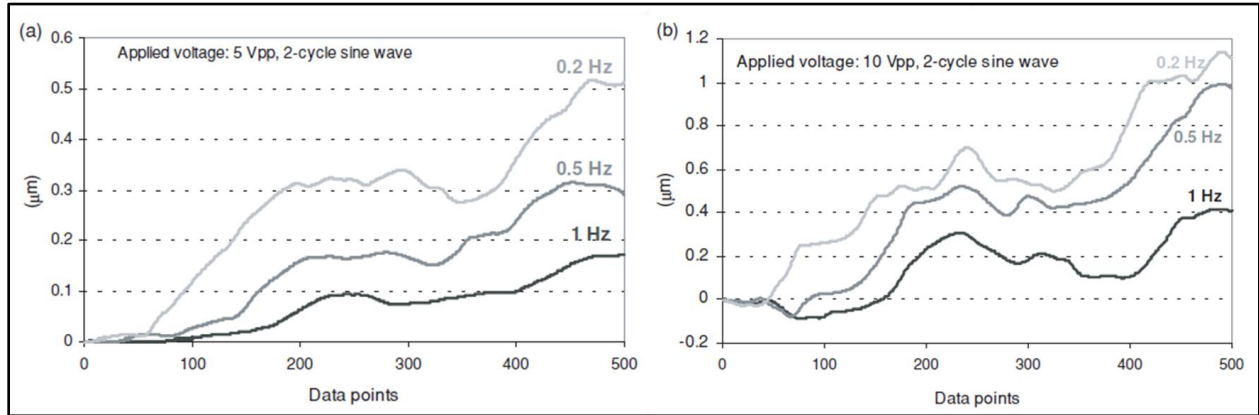


Figure 1.11 Surface displacement amplitude within cartilage generated by 1, 0.5 and 0.2Hz excitation.

Since the streaming potential and other electro-kinetic effects in cartilage are directly related to proteoglycan density, the application of an electric field in cartilage combined with optical reflectometry measurements was suggested to be used as sensitive indicator of cartilage viability.

As was mentioned above, changes in tissue electrical properties reflect the changes in tissue physiology [17]. This principle has been used to identify or monitor the presence of various illnesses including tumors through increased conductivity [33]. Tumors generally have higher water content than normal tissues because of cellular necrosis but also irregular and fenestrated vascularization. In addition, differences may exist in the membrane structure. The increased conductivity of tumors therefore affects the motion of particles and fluids under influence of electric field being applied to suspicious tissues. One of the potential methods for early detection of pathology through these changes in electro-kinetic properties of tissue on the cellular level was reported in [34]. It was experimentally shown that malignant transformation of cells is correlated to the changes in the FCD on cell membranes. In another publication, it was reported

that within the tumor, FCD was significantly larger than the one on cell membranes within normal tissue at different pH levels [35]. Ultrasound has also showed a similar correlation of FCD in the extracellular matrix with physiological and pathological changes in tissue [36]. Dolowy has demonstrated that charges on cell surfaces increase during tumorogenesis and decreases during necrosis [37].

In parallel to observations in [14] that tissue electrical conductivity is higher at low frequency levels, it has been found that the difference in electrical conductivity values for malignant and normal tissues is much higher in the lower frequency range, as reported in Haemmerich et al [38]. It was shown that although the conductivity of malignant tissue is higher at all frequencies, the difference is much higher at lower frequencies of the applied electric field.

These previous studies and thesis author's investigations demonstrate that a promising emerging biophotonic candidate, being capable to detect and visualize this difference through electric field induced changes, may be optical coherence tomography (OCT). It demonstrates a promising potential of developing a technique for monitoring the fixed charge density changes within tissues through their electro-kinetic responses with OCT signal amplitude and phase analysis. For this purpose, changes in tissue structure induced by EKP are further investigated in this study through the amplitude and phase changes in optical coherence tomography signal.

## **1.5 Optical coherence tomography**

Optical coherence tomography is a non-invasive imaging technique that provides real-time one-, two- and three-dimensional images of samples with micrometer resolution [39]. By mapping the local reflectivity, OCT visualizes the morphology of the sample. In addition, functional properties such as birefringence, motion, or the distributions of certain substances can

be detected with high spatial resolution [40]. Its main field of application is biomedical imaging and diagnostics. In ophthalmology, OCT is accepted as a clinical standard for diagnosing and monitoring the treatment of a number of retinal diseases, and OCT is becoming an important instrument for clinical cardiology. New applications are emerging in various medical fields, such as early-stage cancer detection, surgical guidance, and the early diagnosis of musculoskeletal diseases.

OCT measures the depth-resolved reflectivity of scattering materials by detecting backscattered light [41]. Every OCT system probes the sample with a beam of light, and lets the reflections interfere with a reference beam originating from the same light source. From the resulting interference signal, one can derive the reflectivity profile along the beam axis. This one-dimensional depth scan is called the A-scan, in analogy to ultrasound imaging. OCT systems perform many adjacent A-scans in order to create two- or three-dimensional images of the sample.

A-scans can be acquired either in the time domain (TD) or in the frequency domain (FD). In this study the frequency domain OCT is used, in particular, swept source SS-OCT [42].

A SS-OCT system acquires A-scans with a fixed reference path by measuring the spectral response of the interferometer [Figure 1.12]. With a tunable narrowband light source, a sweep over a broad range of optical frequencies is performed (which led to the term swept source OCT) to measure the power then at the output with a single photo-detector. The information is then encoded as an interferogram in optical frequency space; the interferogram is a sum of oscillations with different periods corresponding to reflections from different depths. A Fourier transform of this interferogram reveals the reflectivity profile of the sample.

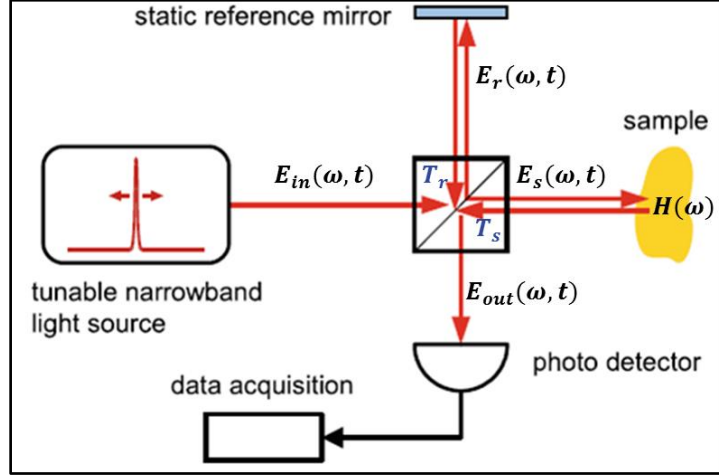


Figure 1.12 Schematic presentation of swept-source optical coherence tomography.

Mathematically OCT can be described in terms of the electric field  $E(\omega, t)$  expressed as a complex exponential [43]:

$$E(\omega, t) = s(\omega)e^{-i(\omega t + kz)} \quad (8)$$

with source field amplitude spectrum  $s(\omega)$ , frequency  $\omega$  and time variation  $t$ . The second term in the exponential, in terms of wavenumber  $k$  and distance  $z$ , accounts for phase accumulated throughout interferometer. The interferometer measures only the relative output phase between the two optical paths. Besides, the input phase is arbitrary. Therefore, the phase term can be dropped from the input electric field. The field in each part of interferometer in Figure 1.11 is denoted by subscripts as  $E_{in}$ ,  $E_{out}$ ,  $E_r$  and  $E_s$  corresponding to optical fields in the input, output, reference and sample arms, respectively. The reference mirror is assumed to be ideal and the beam splitter has reference and sample arm intensity transmittance  $T_r$  and  $T_s$ , respectively, such as  $T_r + T_s = 1$ . The tissue sample has a frequency domain response function  $H(\omega)$  that describes the overall reflection from all internal structures distributed in the  $z$  direction within the tissue and accounts for phase accumulation therein:

$$H(\omega) = \int_{-\infty}^{\infty} r(\omega, z) e^{i2n(\omega, z)\frac{\omega z}{c}} dz \quad (9)$$

where the function  $r(\omega, z)$  is the backscattering coefficient from the sample structural features, and  $n(\omega, z)$  is the frequency dependent, depth varying group refractive index. The exponential term accounts for phase accumulated by the multiple optical paths within the sample.

Therefore, the component optical fields in interferometer are given in terms of the input field  $E_{in}$  [43]:

$$E_{in}(\omega, t) = s(\omega)e^{-i\omega t} \quad (10)$$

$$E_r(\omega, t) = \sqrt{T_r T_s} E_{in}(\omega, t) \quad (11)$$

$$E_s(\omega, t) = \sqrt{T_r T_s} E_{in}(\omega, t) H(\omega) \quad (12)$$

$$E_{out}(\omega, t) = E_r(\omega, t) + E_s(\omega, t) \quad (13)$$

These equations assume that the interferometer is being operated in air. It is also noted that the frequency domain product of the sample response function and input field is equivalent to the convolution of the response function  $H(\omega)$  with the input field  $E_{in}$  in the time domain [44].

Optical detectors are square law intensity detection devices. The recorded intensity is proportional to a time average over the electric field multiplied by its complex conjugate:

$$I(\omega) = \langle E_{out}(\omega, t) E_{out}^*(\omega, t) \rangle \quad (14)$$

where the angle brackets denote a time-average:

$$I(\omega) = \lim_{T \rightarrow \infty} \frac{1}{2T} \int_{-T}^T E_{out}(\omega, t) E_{out}^*(\omega, t) dt \quad (15)$$

After substitution of (11) into (12) the intensity becomes a sum of three terms:

$$I(\omega) = \langle E_s E_s^* \rangle + \langle E_r E_r^* \rangle + 2Re\{\langle E_s E_r^* \rangle\} \quad (16)$$

The first two terms can be identified as “self-reference,” whereas the last term is the real part of the complex “cross-interference.” Making the relevant substitutions from equations (10)-(12) and substituting for the field spectrum  $s(\omega)$  a corresponding intensity spectrum  $S(\omega) = |s(\omega)|^2$ , the recorded intensity spectrum is given by:

$$I(\omega) = T_r T_s S(\omega) |H(\omega)|^2 + T_r T_s S(\omega) + 2T_r T_s \text{Re}\{S(\omega) H(\omega)\} \quad (17)$$

First and second “self-reference” terms of the equation (17) give rise to artificial signals at and near the zero path length position, since the distance between reflectors in the tissue sample is typically much smaller than the distance between the sample reflectors and the reference arm path length. If the reference mirror reflectivity is adjusted to be sufficient so that the amplitude of the “self-reference” terms is very small compared to “cross-interference” terms, the “self-reference” terms of (17) can be neglected [45]:

$$I(\omega) = 2T_r T_s S(\omega) r(\omega, z) \cos\left(2n(\omega, z) \frac{\omega z}{c}\right) \quad (18)$$

Figure 1.13 represents the recorded intensity  $I(\omega)$  in the form of interferogram for the number of

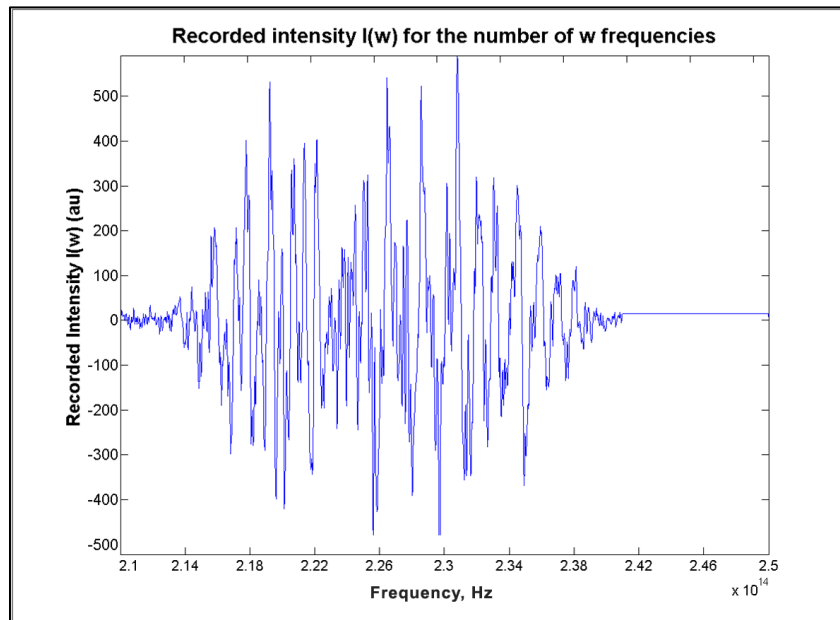


Figure 1.13 Recorded intensity  $I(\omega)$  for the number of  $\omega$  frequencies.

$\omega$  frequencies for SS-OCT system (Swept Source Laser Model # SL1325-P16, Thorlabs Inc. Newton, NJ) that has a central wavelength of 1310 nm and the spectral bandwidth of 70 nm. This interferogram is a sum of oscillations with different periods corresponding to reflections from different depths. An inverse Fourier transform of this interferogram reveals the reflectivity as a complex (amplitude and phase) function of depth, i.e. depth reflectivity profile of the sample:

$$X(m) = \frac{1}{N} \sum_{k=0}^{N-1} I(\omega_k) e^{j\frac{2\pi km}{N}}, \quad m = 0, 1, 2, \dots, N-1 \quad (19)$$

where actual depth  $z$  is represented by tissue evenly distributed layers  $m$ .

The amplitude of the OCT signal backscattered from the 2.25mm in depth biological tissue sample is shown in Figure 1.14. It was calculated by taking the absolute value  $|X(m)|$  of (17) from recorded intensity values shown in Figure 1.13.

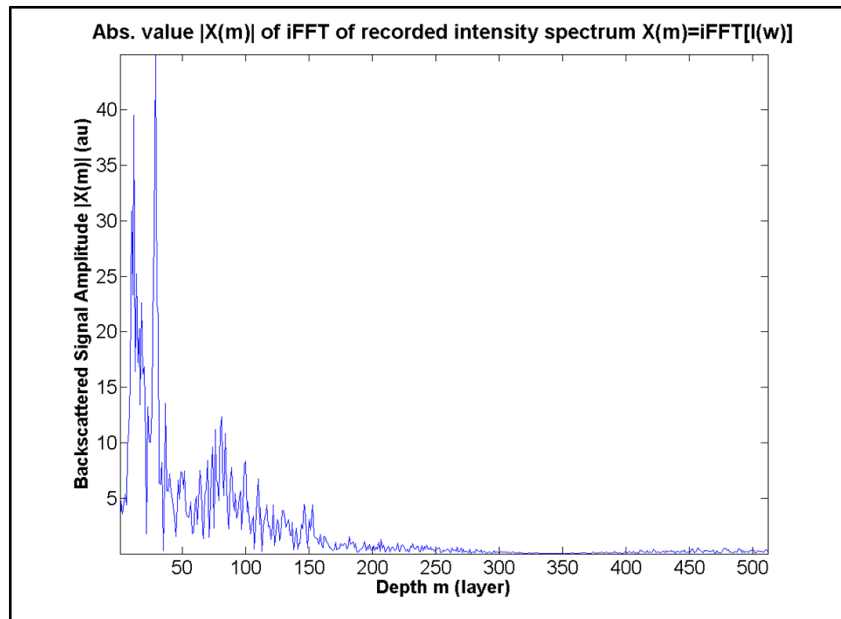


Figure 1.14 Amplitude of the OCT signal backscattered from the biological tissue sample.

There exists a variety of methods of phase extraction from interferograms. The phase shifting approach [46] is a popular technique for phase estimation; however, its application is limited by the requirement of multiple frames. For phase estimation using a single frame, several methods have been proposed, including Fourier transform [47], regularized phase tracking [48], high-order ambiguity function [49], windowed Fourier Transform [50], dilating Gabor transform [51], Wavelet transform [52], and Wigner-Ville distribution [53]. The Fourier transform method is widely used. After inverse Fourier transform  $X(m)$  of the interferogram, a four-quadrant inverse tangent of imaginary to real  $X(m)$  parts ratio is calculated for phase estimation. The example of phase retrieval from interferogram in Figure 1.13 is shown in Figure 1.15 where phases for each depth layer  $m$  were calculated and then unwrapped.

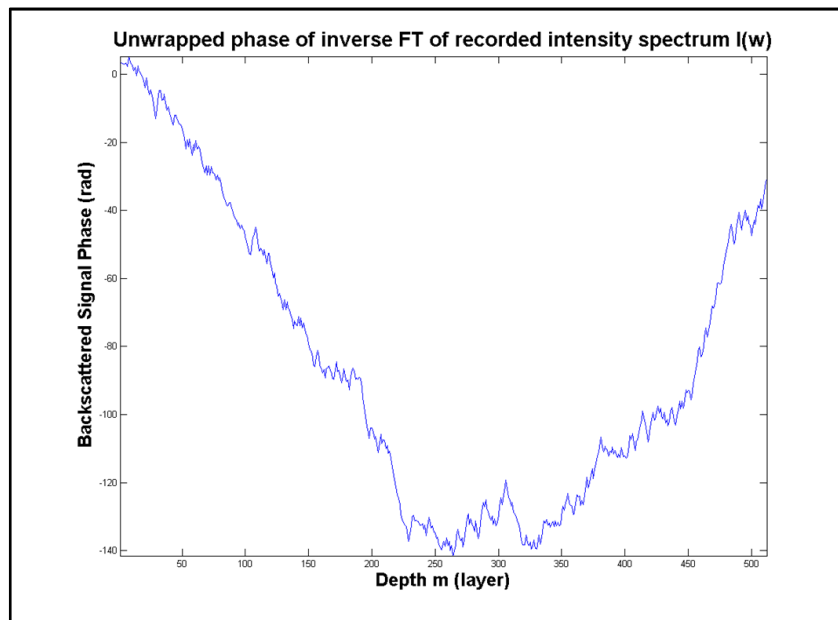


Figure 1.15 Phase of the OCT signal backscattered from the biological tissue sample.

The periodic electric field applied to biological tissue in our previously reported one-dimensional experiments demonstrated to influence the OCT signal amplitude significantly [54]. The amplitude reflected the periodic change of the polarity of external electric field with the

same frequency as the applied field. These oscillations were clearly seen because the field shifted the tissue interstitial fluids periodically, which changed light scattering and absorbance by affecting the mutual alignment of collagen fibrils in tissue [55].

## **1.6 Thesis objectives and outline**

The goal of this research is to develop a method to obtain high-spatial-resolution information about the electro-kinetic response of biological tissues by combining optical coherence tomography (OCT) and low frequency external electric field.

Chapter 2 contains a journal manuscript on the development of electrically induced optical changes (EIOC) imaging method. In this method, the goal is to image the electro-kinetic response of heart tissue by utilizing the amplitude of OCT signal. Manuscript is organized in two parts containing 1D and 2D investigations. The first part (1D) was originally done by Krzysztof Wawrzyn during his undergraduate research project at Ryerson University. It is devoted to detection of periodic variations in the amplitude of OCT signal caused by the periodic external AC electric field being exposed to a heart tissue and development of detected signal processing method. The second part (2D) was done by the author of this thesis. EIOC images related to the electro-kinetic properties of tissue were obtained and compared with structural OCT images.

Chapter 3 is focused on further investigation of EKP in tissues through the phase changes of OCT signal. It contains a journal manuscript on the reconstruction the electro-kinetic response of biological tissues through EIOC phase images. Since the resulting phase signal was corrupted by system phase noise, an advanced signal processing method was developed to obtain the images of electrically induced phase changes.

Finally, a summary of the findings of this thesis is provided in Chapter 4 as well as suggestions for a future work.

## References

- [1] E. Neumann, M. Schaeferriidder, Y. Wang, P. Hofschneider, “Gene-transfer into mouse lyoma cells by electroporation in high electric-fields,” *EMBO J.* 1, 841-845 (1982).
- [2] A. D. Waller, “A demonstration on man of electromotive changes accompanying the heart's beat,” *J. Physiol. (Lond)* 8 (5), 229–234 (1887).
- [3] E. Niedermeyer and F. L. da Silva, “Electroencephalography: Basic Principles, Clinical Applications, and Related Fields,” Lippincot Williams & Wilkins (2004).
- [4] R. C. Lee, D. J. Canaday, H. Doong, “A review of the biophysical basis for the clinical application of electric fields in soft-tissue repair,” *J. Burn. Care Rehabil.* 14 (3), 319-335 (1993).
- [5] D. N. Rushton, “Electrical stimulation in the treatment of pain Disability and Rehabilitation,” 24 (8), 407-415 (2002).
- [6] B. R. Durling, “The kidney”, *Physiology*, ed. by RM Berne, MN Levy, pp. 821-92, St. Lois, MO, Mosby, 1165 pp. (1983).
- [7] L. A. Geddes, L. E. Baker, “The specific resistance of biological material: a compendium of data for the biomedical engineer and physiologist,” *Med. Biol. Eng.* 5, 271–293 (1967).
- [8] A. Sances, J. B. Myklebust, S. J. Larson, J. C. Darin, T. Swiontek, “Experimental electrical injury studies,” *J. Trauma* 21(8), 589–597 (1981).

- [9] D. G. Gaylor, A. Prakah-Asante, R. C. Lee, "Significance of cell size and tissue structure in electrical trauma," *J. Theor. Biol.* 133, 223–237 (1988).
- [10] T. Y. Tsong, "Electroporation of cell membranes," *Biophys J.* 60(2), 297-306 (1991).
- [11] D. Miklavcic, N. Pavselj, and F. X. Hart, "Electric properties of tissues", in *Wiley Encyclopedia of Biomedical Engineering*, Wiley (2009).
- [12] S. Grimnes and O. G. Martinsen, "Bioimpedance & Bioelectricity Basics," San Diego, CA: Academic Press (2000).
- [13] K. R. Foster and H. P. Schwan, "Dielectric properties of tissues and biological materials: a critical review," *Crit. Rev. Biomed. Eng.* 17, 25–104 (1989).
- [14] J. P. Reilly, "Applied Bioelectricity, From Electrical Stimulation to Electropathology," New York: Springer-Verlag (1998).
- [15] R. Pethig, "Dielectric and Electronic Properties of Biological Material," New York: Wiley (1979).
- [16] L. A. Geddes and L. E. Baker, "The specific resistance of biological material - a compendium of data for the biomedical engineer and physiologist," *Med. Biol. Eng.* 5, 271–293 (1967).
- [17] E. Pacelat, R. Magjarevic, and V. Isgum, "Measurement of electrode-tissue interface characteristics during high current transcranial pulse electrical stimulation," *Measurement* 27, 133–143 (2000).

- [18] M. Noshiro, T. Morimoto, H. Nagao, and H. Matsuda, "Electrical impedance in the lower limbs of patients with Duchenne muscular dystrophy: a preliminary study," *Med. Biol. Eng. Comput.* 31, 97–102 (1993).
- [19] K. Thethi, P. Jurasz, A. J. MacDonald, A. D. Befus, S. F. Man, and M. Duszyk, "Determination of cell surface charge by photometric titration," *Journal of Biochemical and Biophysical Methods*, 34(2), 137-145 (1997).
- [20] I. Gersh, and H. R. Catchpole, "The Nature of Ground Substance of Connective Tissue," *Perspectives in Biology and Medicine* 3, 282–319 (1960).
- [21] A. V. Delgado, F. González-Caballero, R. J. Hunter, L. K. Koopal, and J. Lyklema, "Measurement and interpretation of electrokinetic phenomena," *Journal of Colloid and Interface Science*, 309(2), 194-224 (2007).
- [22] J. Lyklema, "Fundamentals of Interface and Colloid Science," Academic Press (2005).
- [23] M. von Smoluchowski, in: "Handbuch der Electricität und des Magnetismus (Graetz)", vol. II, Barth, Leipzig, 1921, p. 366.
- [24] C. Katnik and R. Waugh, "Electric fields induce reversible changes in the surface to volume ratio of micropipette-aspirated erythrocytes," *Biophysical Journal* 57(4), 865-875 (1990).
- [25] S. Méthot, V. Moulin, D. Rancourt, M. Bourdages, D. Goulet, M. Plante, F. A. Auger, and L. Germain, "Morphological changes of human skin cells exposed to a DC electric field in vitro using a new exposure system," *Canadian Journal of Chemical Engineering* 79(4), 668-677 (2001).

- [26] C. A. Erickson, and R. Nuccitelli, "Embryonic fibroblast motility and orientation can be influenced by physiological electric fields," *Journal of Cell Biology* 98(1), 296-307 (1984).
- [27] O. Doganay and Y. Xu, "The effect of electric current in biological tissues on ultrasound echoes," *Proceedings of IEEE Ultrasonics Symposium* 2103-2106 (2009).
- [28] O. Doganay and Y. Xu, "Electric-field induced strain in biological tissues," *Journal of the Acoustical Society of America* 128(5), EL261-EL267 (2010).
- [29] O. Doganay and Y. Xu, "Reversibility of electric-field induced mechanical changes (EIMC) in soft tissues," *IEEE TUFFC-04263-2011.R1* (2012).
- [30] E. H. Frank, A. J. Grodzinsky, "Cartilage electromechanics - I. Electrokinetic transduction and the effects of electrolyte pH and ionic strength," *Journal of Biomechanics* 20(6), 615-27 (1987).
- [31] E. H. Frank, A. J. Grodzinsky, "Cartilage electromechanics - II. A continuum model of cartilage electrokinetics and correlation with experiments," *Journal of Biomechanics* 20(6), 629-39 (1987).
- [32] J. I. Youn, T. Akkin, and T. E. Milner, "Electrokinetic measurement of cartilage using differential phase optical coherence tomography," *Physiological Measurement*, 25(1), 85-95 (2004).
- [33] D. Haemmerich, S. T. Staelin, J. Z. Tsai, S. Tungjitkusolmun, D. M. Mahvi, and J. G. Webster, "In vivo electrical conductivity of hepatic tumours," *Physiol. Meas.* 24, 251-260 (2003).

- [34] B. Szachowicz-Petelska, I. Dobrzyska, Z. Figaszewski, and S. Sulkowski, "Changes in physico-chemical properties of human large intestine tumour cells membrane," *Molecular and Cellular Biochemistry*, 238(1-2), 41-47 (2002).
- [35] B. Szachowicz-Petelska, I. Dobrzyska, S. Sulkowski and Z. Figaszewski, "Characterization of the cell membrane during cancer transformation," *Journal of Environmental Biology*, 31(5), 845-850 (2010).
- [36] M. F. Insana, C.P. Barakat, M. Sridhar, K. K. Lindfors, "Viscoelastic imaging of breast tumor microenvironment with ultrasound," *Journal of Mammary Gland Biology and Neoplasia* 9(4), 393–404 (2004).
- [37] K. Dolowy, "Biochemistry of cell surface," *Progr. Surf. Sci.* 15, 245-368 (1984).
- [38] D. Haemmerich, D. J. Schutt, A. W. Wright, J. G. Webster, and D. M. Mahvi, "Electrical conductivity measurement of excised human metastatic liver tumors before and after thermal ablation," *Physiol. Meas.* 30, 459 (2009).
- [39] D. Huang, E. A. Swanson, C. P. Lin, J. S. Schuman, W. G. Stinson, W. Chang, M. R. Hee, T. Flotte, K. Gregory, C. A. Puliafito, and J. G. Fujimoto, "Optical coherence tomography," *Science* 254, 1178-1180 (1991).
- [40] S. Marschall, B. Sander, M. Mogensen, T. M. Jørgensen, P. E. Andersen, "Optical coherence tomography-current technology and applications in clinical and biomedical research," *Anal. Bioanal. Chem.* 400(9), 2699-720 (2011).

- [41] J. G. Fujimoto, C. Pitris, S. A. Boppart, and M. E. Brezinski, "Optical coherence tomography: An emerging technology for biomedical imaging and optical biopsy," *Neoplasia* 2(1-2), 9-25 (2000).
- [42] S. R. Chinn, E. A. Swanson, J. G. Fujimoto, "OCT using a frequency-tunable optical source," *Opt. Lett.* 22(5), 340–342 (1997).
- [43] P. Tomlins and R. Wang "Theory, developments and applications of optical coherence tomography," *J. Phys. D* 38 (2005).
- [44] P. Hariharan, "Optical interferometry," 2nd edition, New York Academic (2003).
- [45] J. A. Izatt and M. A. Choma, "Theory of optical coherence tomography," in "OCT Technologies and Applications," ed. W. Drexler and J. G. Fujimoto, Springer, 1346 pp. (2008).
- [46] K. Creath, "Phase-measurement interferometry techniques" in ed. E. Wolf "Progress in optics" 26 Amsterdam: Elsevier, 349–393 (1988).
- [47] M. Takeda, H. Ina, S. Kobayashi, "Fourier transform methods of fringe pattern analysis for computer based topography and interferometry," *J. Opt. Soc. Am.* 72, 156–160 (1982).
- [48] M. Servin, J. L. Marroquin, and F. J. Cuevas, "Demodulation of a single interferogram by use of a two-dimensional regularized phase-tracking technique," *Appl. Opt.* 36, 4540–48 (1997).
- [49] S. S. Gorthi and P. Rastogi, "Numerical analysis of fringe patterns recorded in holographic interferometry using high-order ambiguity function," *J. Mod. Opt.*, 56 (8), 949-954 (2009).

- [50] Q. Kemao, "Windowed Fourier transform for fringe pattern analysis," *Appl. Opt.*, 43 (13) 2695-2702 (2004).
- [51] J. Zhong, J. Weng, "Dilating Gabor transform for the fringe analysis of 3-D shape measurement," *Optical Engineering* 43 (4), 895-899 (2004).
- [52] L. R. Watkins, S. M. Tan, and T. H. Barnes, "Determination of interferometer phase distributions by use of wavelets," *Opt. Lett.* 24, 905-907 (1999)
- [53] G. Rajshekhar, S. S. Gorthi, P. Rastogi, "Adaptive window Wigner-Ville-distribution-based method to estimate phase derivative from optical fringes," *Opt. Lett.* 34 (20), 3151-3153 (2009).
- [54] K. Wawrzyn, B. Vuong, M. Harduar, V. Yang, V. Demidov, V. Toronov, and Y. Xu, "Monitoring Electric Current in Biological Tissues by Optical Coherence Tomography," in *Biomedical Optics and 3-D Imaging*, OSA Technical Digest (Optical Society of America, 2012), paper BW2A.4.
- [55] H. J. Swatland, "Basic Science for Carcass Grading," *VI Congresso Brasileiro de Ciencia e Tecnologia de Carnes*, 6, 119 (2011).

## **2. Imaging the electro-kinetic response of biological tissues by using the amplitude of optical coherence tomography**

**The results of this work were reported in the following paper:**

K. Wawrzyn, **V. Demidov**, B. Vuong, M. K. Harduar, C. Sun, V. X. D. Yang, O. Doganay, V.

Toronov and Y. Xu, "Imaging the electro-kinetic response of biological tissues with optical coherence tomography," *Optics Letters* 38(14), pp. 2572-2574 (2013).

# Imaging the electro-kinetic response of biological tissues with OCT

K. Wawrzyn,<sup>1,†</sup> V. Demidov,<sup>1,†</sup> B. Vuong,<sup>2</sup> M. K. Harduar,<sup>2</sup> C. Sun,<sup>2,3</sup>  
V. X. D. Yang,<sup>2,4</sup> O. Doganay,<sup>1</sup> V. Toronov,<sup>1</sup> and Y. Xu<sup>1,\*</sup>

<sup>1</sup>*Department of Physics, Ryerson University, Toronto, Canada*

<sup>2</sup>*Department of Electrical and Computer Engineering Ryerson University, Toronto, Canada*

<sup>3</sup>*Department of Medicine, University of Toronto*

<sup>4</sup>*Division of Neurosurgery, University of Toronto, Toronto, Canada*

\*Corresponding author: [yxu@ryerson.ca](mailto:yxu@ryerson.ca)

Received April 22, 2013; revised June 6, 2013; accepted June 10, 2013;  
posted June 14, 2013 (Doc. ID 189149); published July 12, 2013

## Abstract

We demonstrate the feasibility of using optical coherence tomography (OCT) to detect and image an electro-kinetic response: Electric-Field Induced Optical Changes (EIOC) in soft biological tissues. A low-frequency electric field was applied to *ex vivo* samples of porcine heart tissues while OCT signals were acquired continuously. Experimental results show that the amplitude of the OCT signal changes is proportional to the amplitude and inversely proportional to the frequency of the applied electric field. We show that the non-conductive component of the sample was eliminated in the normalized EIOC image. To the best of our knowledge, this is the first time a two-dimensional image related to the electro-kinetic response of soft tissues is obtained with depth resolution. Since electro-kinetic properties can change during cancerogenesis, EIOC imaging can potentially be used for cancer detection.

© 2013 Optical Society of America.

OCIS codes: (110.4500) Optical coherence tomography; (170.2655) Functional monitoring and imaging; (170.6935) Tissue characterization; (170.7180) Ultrasound diagnostics.

<http://dx.doi.org/10.1364/OL.38.002572>

## 2.1 Introduction

Many molecules, such as proteins and Glycosaminoglycan (GAG), on cell surfaces [1] or in the extracellular matrix of biological tissues have net electric charges, which can be described by a fixed charge density (FCD). Fixed charges cannot move around freely within the tissues when subjected to an electric field and therefore, do not contribute to conductivity. However, by interacting with the mobile ions in interstitial fluid the fixed charges are responsible for various electro-kinetic phenomena (EKP) [2], which are the motion of particles and fluids under the influence of the electric field [3]. EKP depend on many tissue properties, such as the fixed charge density, electrical conductivity, local pH variations, hydraulic permeability, ion diffusivity, and stiffness [4]. EKP have been observed using optical microscopy in colloids, blood, and cell cultures, such as changes in cellular shape [5], orientation [6] and migration (galvanotaxis) [7]. Frank and Grodzinsky measured the mechanical stress when the electric field was applied to the articular cartilage (a high FCD tissue) confined between two rigid plates [8,9]. Similarly, differential-phase reflectometry was used to monitor the electric field induced surface displacements of the cartilage tissue [10]. It was demonstrated that the magnitude of these surface displacements increased with amplitude and decreased with the frequency of the applied electric field.

EKP of various soft biological tissues have not been imaged with depth resolution until recently [11-13]. Ultrasound was used to image the electric-field induced *mechanical* changes

(EIMC) in bulk tissues including deformation and strain one-dimensionally [12]. These EIMC in soft biological tissues were related to EKP [13].

OCT allows for non-invasive, high-resolution and depth-resolved imaging of internal tissue structure [14]. However standard structural OCT imaging cannot detect early pathological changes [15]. To investigate EKP in soft biological tissue, in this study we demonstrate that EKP can be imaged through the amplitude changes of OCT signals. To the best our knowledge, this is the first time a two-dimensional image related to the electro-kinetic response of soft tissues is obtained with depth resolution.

## 2.2 Experimental Setup

The experimental setup is shown in Fig. 1. The experimental protocol was similar to that of previous studies with ultrasound [11]. The tricuspid valves from the right ventricle of fresh porcine hearts were used as specimens.

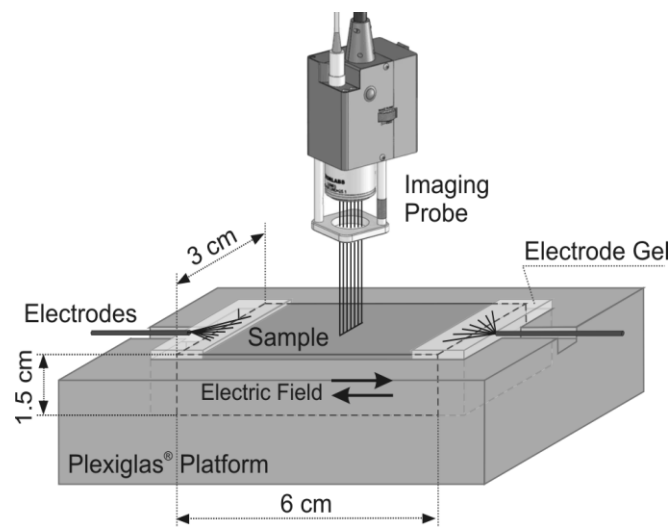


Figure 2.1 Diagram of the experimental setup.

Rectangular tissue sample ( $\sim 6 \times 3 \times 1.5$  cm) was clamped into a Plexiglas® frame to reduce random mechanical motion. Electrodes made of 24 AWG PVC hook-up 7x32 tinned copper wires (Copper Industries Belden Division, Richmond, IN) were placed 6 cm apart on the opposite sides of the surface of the sample (Fig. 2.1). To improve the electrical contact each electrode was covered by the electrode gel Spectra 360 (Parker Laboratories, Inc. Fairfield, NJ). A synthetic function generator (Stanford Research, CA, model DS335) was used to generate square-waves of 1-10 V amplitude and of 0.1-1.0 Hz frequency, which were applied to the electrodes. In order to minimize the effects of the temperature changes the specimen was left at room temperature for 5 hours before the experiment. The OCT system (Swept Source Laser Model # SL1325-P16, Thorlabs Inc. Newton, NJ) had a central wavelength of 1310 nm and the spectral bandwidth of 70 nm. The bandwidth was measured using the optical spectrum analyzer. The optical axial and transverse resolutions of the system were 10.8  $\mu\text{m}$  and 25  $\mu\text{m}$  (in air), respectively.

## **2.3 Results**

### **2.3.1 1D-Mode**

The electro-kinetic response of the tissue was initially investigated with M-mode OCT. 1024 consecutive M-mode A-scans with axial scan rate 16 kHz were acquired and then averaged to 1 A-scan per second. Figure 2(a) shows the time course (480 seconds) of the relative amplitude of the OCT signal normalized by the signal amplitude for one depth averaged over time. The AC voltage was applied only during the interval from 120 s to 300 s, as indicated by the solid box. The amplitude of the OCT signal oscillates with the applied voltage. To study the linear response of the tissue to the applied field, Savitzky-Golay algorithm (sgolay function in Matlab, Mathworks, Natick, MA) was used to eliminate the slow trend (which is common in

conventional optical swept sources [16]) in the signal [Fig. 2(a)]. The motivation for this de-trending procedure was the elimination of the spurious frequencies in the spectrum of the signal from the trend. To quantify the electric-field induced *optical* changes (EIOC), a Fourier transform was first applied to the de-trended signal during the interval of AC application. Then the magnitude of the Fourier spectrum at the frequency of the applied electric current [Fig. 2(c)] was used to represent the magnitude of EIOC. To investigate the dependence of EIOC on the applied voltage, 0.1 Hz AC square waves with various amplitudes from 1 to 10 V were applied to the sample.

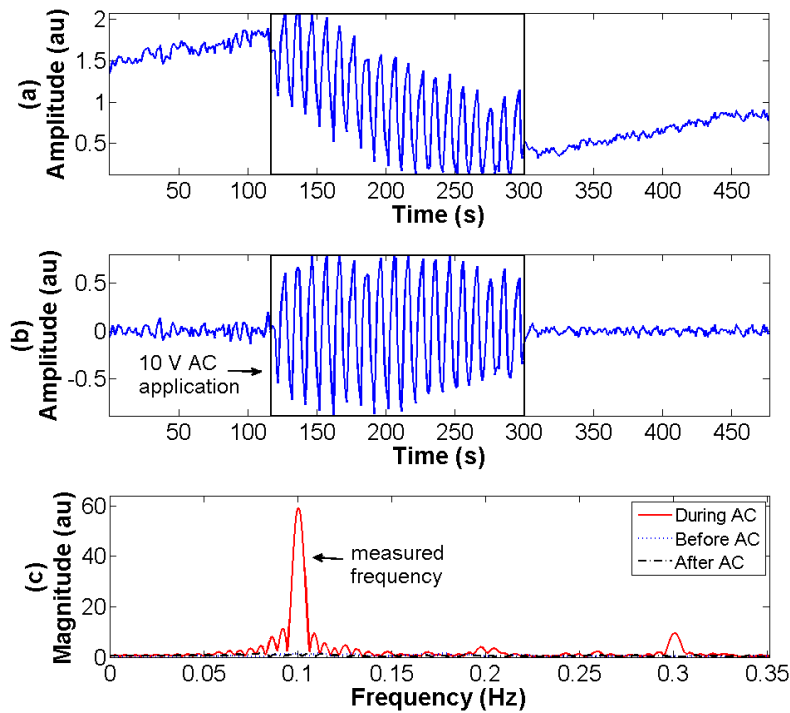


Figure 2.2 (a) The time course of a typical OCT signal acquired on a sample before, during (inside the solid square), and after the AC voltage application. (b) same time course after de-trending. (c) Fourier spectrum of 3 portions of the signal.

To investigate frequency dependence of EIOC, 10 V AC square waves were applied to the sample by varying frequencies from 0.1 to 1 Hz. In order to compare the changes in the OCT

signal, Fourier spectra peak values for the selected range of sample depths were averaged, and then converted to the percentage of amplitude change of OCT signals. The range of depths was selected from the surface of the sample to the depth below which the Fourier spectra peaks started to be dominated by noise. The EIOC amplitude dependence on the voltage is shown in Fig. 3(a), where a linear regression fit demonstrates that the EIOC magnitude increases linearly with the applied voltage. The EIOC amplitude dependence on the frequency is shown in Fig. 3(b). From Fig. 3(b) one can see that the EIOC magnitude is inversely proportional to the frequency of the applied electric field.

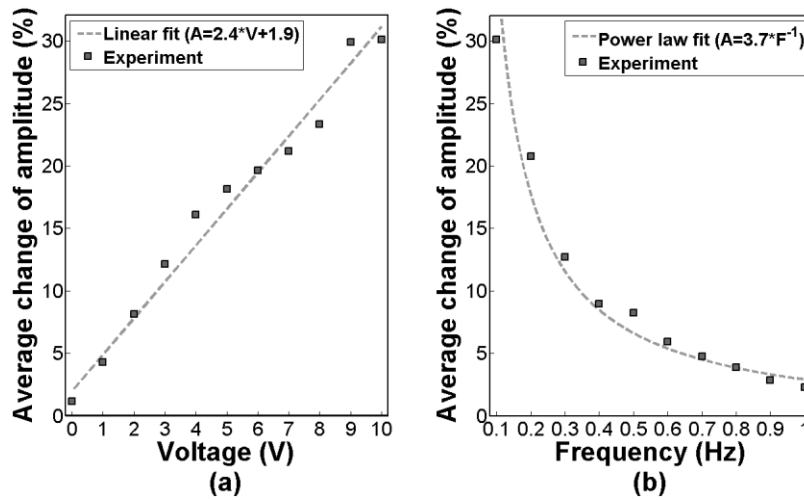


Figure 2.3 Dependence of average EIOC amplitude on: (a) the amplitude and (b) the frequency of the applied voltage.

### 2.3.2 2D-Mode

To investigate EIOC in 2D, a series of B mode OCT images ( $3 \times 3$  mm with  $1024 \times 512$  pixels) were acquired with the rate of 0.064 s per image and 1 s between images. The 10 V, 0.1 Hz square-wave voltage was applied to the tissue during the time interval from 120 s to 300 s. The signal processing technique was the same as in the 1D case. Fig. 4 illustrates the 2D image processing technique. For each  $(x,y)$  pixel of a B-mode OCT image (1024 by 512 pixels), the

temporal profile  $A(t)$  [such as the plot in Fig. 2(a)] of the corresponding OCT signal during the application of external electric field ( $t_{\text{start}}=120$  s,  $t_{\text{end}}=300$  s) was extracted from the  $A(x,y,t)$  matrix.

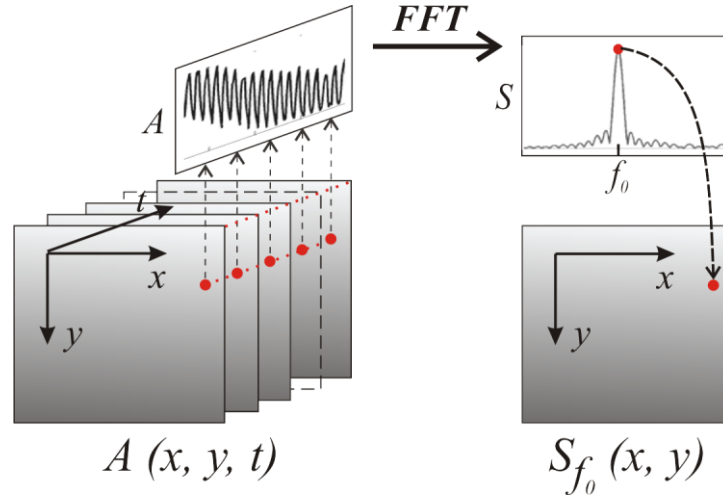


Figure 2.4 Illustration of the EIOC image processing algorithm.

Then a fast Fourier transform (FFT) was applied to the de-trended signals to obtain the spectral magnitudes  $S_f(x,y)$ . Lastly,  $S_f(x,y)$ , at the frequency  $f_0=0.1$ Hz of the applied electric field were mapped to the corresponding  $(x,y)$  pixels to construct an un-normalized EIOC image. The total processing time for the 2D case was 12 minutes on an AMD Bulldozer® 4.0 GHz 8-core system in Matlab.

In order to verify the ability of the technique to image the electro-kinetic response of tissues, a 1 mm diameter dielectric optical fiber was inserted into the middle of the sample at an arbitrary angle. Figs. 5(a) and (b) display the structural and the un-normalized EIOC images, respectively. In both Figs. 5(a) and (b), the optical fiber cladding material surrounding the transparent core can be clearly distinguished.

Although no electro-kinetic response can occur in the optical fiber, the fiber is still visible in the EIOC image [Fig. 5(b)] because the background fluctuations of OCT signals gave rise to

non-zero FFT values. In order to eliminate them from the EIOC image, a background image was computed using the FFT magnitude [Fig 2(b)] averaged over all the frequencies except the narrow bands around  $f_0=0.1Hz$  and its corresponding harmonics. Then the EIOC image was divided by the background image, pixel-by-pixel. The result of this normalization is shown in Fig. 5(d).

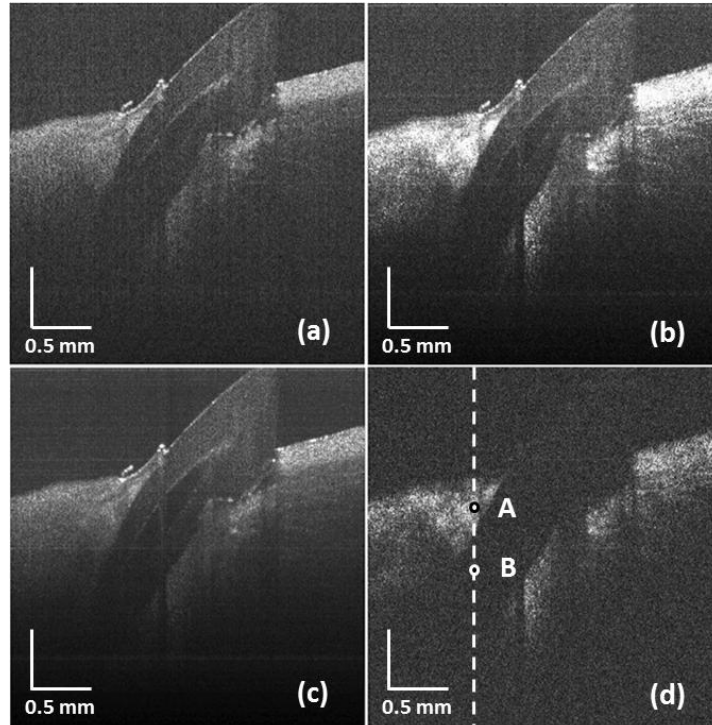


Figure 2.5 (a) Original OCT image; (b) Un-normalized OCT-based EIOC image; (c) EIOC background image during electric field application; (d) OCT-based EIOC image normalized by the EIOC background image during electric field application.

## 2.4 Discussion

One can clearly see that the fiber and a small piece of surface tissue to the left of the fiber in Fig. 5(b) do not appear in Fig. 5(d), which is in agreement with the absence of electric current and electro-kinetic phenomena in them. It can also be concluded that the normalized EIOC image in Fig. 5(d) represents the information related to the local EKP of the tissue, rather than

the one translated from other locations on the light pathway. Because if the EIOC were due to the changes in the path of the forward and backward light propagation, then any EIOC in top layer (for example, point A in Fig 5(d)) will result in the EIOC of the signal under that layer (point B in Fig 5(d)). However, no EIOC of signal in the fiber glass region were detected even though there are significant EIOC in the tissue above it.

## **2.5 Conclusion**

Recently ultrasound imaging was used to investigate EIMC in biological tissues [11-13], including both the irreversible (strain) and reversible changes. In the current study, we report an observation of similar effects using OCT. Since the changes shown in Fig 2(a) are mostly reversible (opposite polarities of the applied voltage cause opposite OCT signal changes), it is unlikely that these changes were due to the strain, which is irreversible [13]. The result that the amplitude of the OCT signal increases with the amplitude [Fig. 3(a)] and decreases with the frequency [Fig. 3(b)] of the applied voltage is consistent with the results of the ultrasound imaging (after a frequency domain analysis of Fig. 5(a) and (c) in [11]) as well as with those of the differential phase reflectometry [10] for the cartilage surface displacements. For the same level of applied electric field to tissue, we found that detected EIOC by OCT have a higher percentage of amplitude change than EIMC by ultrasound. The most likely reason for this is that the wavelengths of light used in OCT (about 1  $\mu\text{m}$ ) are much smaller than the wavelengths of ultrasonic waves (150  $\mu\text{m}$  or greater), therefore OCT is more sensitive to the microscopic changes than the ultrasound. Since both ultrasound-detected EIMC and OCT-detected EIOC are reversible, they may have the same origin, probably due to the deformation of the extracellular matrix and cells, and due to the electrically induced fluid flow as discussed in [13].

This research was supported by NSERC discovery grants (Y. Xu and V. Toronov), CFI (V. X. D. Yang), MITACS (B. Vuong and C. Sun).

<sup>†</sup>The authors contributed equally to this work.

## References

- [1] K. Thethi, P. Jurasz, A. J. MacDonald, A. D. Befus, S. F. Man, and M. Duszyk, "Determination of cell surface charge by photometric titration," *Journal of Biochemical and Biophysical Methods*, 34(2), 137-145 (1997).
- [2] A. V. Delgado, F. González-Caballero, R. J. Hunter, L. K. Koopal, and J. Lyklema, "Measurement and interpretation of electrokinetic phenomena," *Journal of Colloid and Interface Science*, 309(2), 194-224 (2007).
- [3] J. Lyklema, *Fundamentals of Interface and Colloid Science* (Academic Press, 2005).
- [4] W.Y. Gu, W. M. Lai, V. C. Mow, "Transport of multi-electrolytes in charged hydrated biological soft tissues," *Porous Media: Theory and Experiments*, 34, 143-157 (1999).
- [5] C. Katnik and R. Waugh, "Electric fields induce reversible changes in the surface to volume ratio of micropipette-aspirated erythrocytes," *Biophysical Journal*, 57(4), 865-875 (1990).
- [6] S. Méthot, V. Moulin, D. Rancourt, M. Bourdages, D. Goulet, M. Plante, F. A. Auger, and L. Germain, "Morphological changes of human skin cells exposed to a DC electric field in vitro using a new exposure system," *Canadian Journal of Chemical Engineering*, 79(4), 668-677 (2001).

- [7] C. A. Erickson, and R. Nuccitelli, "Embryonic fibroblast motility and orientation can be influenced by physiological electric fields," *Journal of Cell Biology*, 98(1), 296-307 (1984).
- [8] E. H. Frank, A. J. Grodzinsky, "Cartilage electromechanics - I. Electrokinetic transduction and the effects of electrolyte pH and ionic strength," *Journal of Biomechanics*, 20(6), 615-27 (1987).
- [9] E. H. Frank, A. J. Grodzinsky, "Cartilage electromechanics - II. A continuum model of cartilage electrokinetics and correlation with experiments. *Journal of Biomechanics*, 20(6), 629-39 (1987).
- [10] J. I. Youn, T. Akkin, and T. E. Milner, "Electrokinetic measurement of cartilage using differential phase optical coherence tomography," *Physiological Measurement*, 25(1), 85-95 (2004)
- [11] O. Doganay and Y. Xu, "The effect of electric current in biological tissues on ultrasound echoes," in *Proceedings of IEEE Ultrasonics Symposium* (2009), pp. 2103-2106.
- [12] O. Doganay and Y. Xu, "Electric-field induced strain in biological tissues," *Journal of the Acoustical Society of America*, 128(5), EL261-EL267 (2010).
- [13] O. Doganay and Y. Xu, "Reversibility of electric-field induced mechanical changes (EIMC) in soft tissues," *IEEE. TUFFC-04263-2011.R1* (2012, in press).
- [14] J. G. Fujimoto, C. Pitris, S. A. Boppart, and M. E. Brezinski, "Optical coherence tomography: An emerging technology for biomedical imaging and optical biopsy," *Neoplasia* 2(1-2), 9-25 (2000).

[15] A. F. Fercher, W. Drexler, C. K. Hitzenberger, and T. Lasser, "Optical coherence tomography - principles and applications," *Reports on Progress in Physics*, 66(2), 239-303 (2003).

[16] D. C. Adler, R. Huber, and J. G. Fujimoto, "Phase-sensitive optical coherence tomography at up to 370,000 lines per second using buffered Fourier domain mode-locked lasers," *Optics Letters*, 32(6), 626-628 (2007).

### **3. Imaging the electro-kinetic response of biological tissues by using the phase of optical coherence tomography**

**The results of this work were submitted to the Journal of Biomedical Optics:**

**V. Demidov, V. Toronov, Y. Xu, B. Vuong, C. Sun, V. X. D. Yang, and I. A. Vitkin, "Imaging the electro-kinetic response of biological tissues with phase resolved optical coherence tomography," submitted to the Journal of Biomedical Optics in July 2013 (ID 130568).**

# Imaging the electro-kinetic response of biological tissues with phase resolved optical coherence tomography

V. Demidov,<sup>a</sup> V. Toronov,<sup>\*a</sup> Y. Xu,<sup>\*\*a</sup> B. Vuong,<sup>b</sup> C. Sun,<sup>b,c</sup>  
V. X. D. Yang,<sup>a,b</sup> and I. A. Vitkin<sup>d</sup>

<sup>a</sup>*Dept. of Physics,* <sup>b</sup>*Dept. of Electrical and Computer Engineering,*  
*Ryerson University, 50 Gould Street, Toronto, ON, M5B 2K3, Canada;*  
<sup>c</sup>*Dept. of Medicine,* <sup>d</sup>*Depts. of Medical Biophysics and Radiation Oncology,*  
*University of Toronto, 610 University Avenue, Toronto, ON, M5G 2M9, Canada*

## Abstract

The electric field induced optical changes (EIOC) measured by the optical coherence tomography (OCT) reflect the local electro-kinetic properties of the tissue. In this study we developed a method to use the phase of the complex OCT images to map EIOC in tissue samples. Switching the polarity of the electric field induced significant reversible changes in the phase of the complex OCT images. Since the resulting phase was degraded by the noise an advanced signal processing algorithm was developed to obtain the EIOC images. The developed algorithm made it possible to get structural phase images from a standard commercial OCT system, potentially yielding important insights into the local electro-kinetic properties of the tissue.

**Keywords:** phase, optical coherence tomography, electro-kinetic phenomenon, OCT image processing, optical properties of tissue

## 3.1 Introduction

External electric field applied to biological tissue may trigger various effects, related to the electro-kinetic phenomena (EKP).<sup>1</sup> These effects stem from the motion of particles and fluids under the influence of an electric field.<sup>2</sup> EKP depend on many parameters including fixed charge

density, electrical conductivity, local environment (pH variations), hydraulic permeability, ion diffusivity, and stiffness<sup>3</sup>. Applied electric field thus affects cells and biological tissues in various complex ways. Different electric-field induced effects have been investigated using optical microscopy *in vitro* in colloid, blood, and cell culture, to image change in cellular shape,<sup>4</sup> orientation<sup>5</sup> and migration.<sup>6</sup>

Recently EKP has been imaged in various intact soft biological tissues *ex-vivo*.<sup>7-9</sup> In particular, ultrasound was employed to image the electric-field induced mechanical change (EIMC) in bulk tissues including deformation and strain.<sup>8</sup> It was concluded that the EIMC in soft biological tissues were related to EKP.<sup>9</sup> Similarly, the surface displacements of cartilage tissue due to applied electric field were measured using optical reflectometry.<sup>10</sup> It was demonstrated that the surface displacements increased with voltage and were inversely proportional to the frequency of the applied electric field. We have recently reported that exposure of heart tissues to a periodic external AC electric field caused periodic variations in the amplitude of OCT signal.<sup>11</sup> In that study, the amplitude images of electrically induced optical changes (EIOC) related to the electro-kinetic properties of tissue were obtained and compared with structural OCT images. Here, we further investigate electro-kinetic phenomena in soft biological tissues through the phase changes in OCT signal.

OCT measures the depth-resolved reflectivity of scattering materials by detecting backscattered light.<sup>12</sup> An OCT system probes the sample with a beam of light, and interferes the reflections with a reference beam originating from the same light source and reflected off a reference mirror. From the resulting interference signal, one can derive the reflectivity profile along the beam axis. This one-dimensional depth scan is called the A-scan, in analogy to ultrasound imaging. OCT systems perform many adjacent A-scans in order to create two- or

three-dimensional images of the sample. A-scans can be acquired either in the time domain or in the frequency domain. In this study the frequency domain OCT was used, in particular, swept source SS-OCT.<sup>13</sup>

A SS-OCT system acquires A-scans with a fixed reference path (non-moving reference mirror) by measuring the spectral response of the interferometer. With a tunable light source, a sweep over a range of optical frequencies is performed. The interference signal is measured at the output with a photo detector. The information is then encoded as an interferogram in the optical frequency space - a sum of oscillations with different frequencies corresponding to reflections from different depths. An inverse Fourier transform of this interferogram reveals the reflectivity as a complex (amplitude and phase) function of depth, i.e. the depth reflectivity profile of the sample.

In the present study, we demonstrate the ability of SS-OCT to detect the electric field induced changes in biological tissues as a function of time. New imaging schemes and data analysis methodologies are applied to OCT images of tissue to study EKP, in an effort to enrich the information provided by standard OCT. To the best of our knowledge, this is the first time the phase images related to the electro-kinetic properties of tissues are derived and compared with corresponding OCT structural phase images.

## **3.2 Experimental methods**

### **3.2.1 Specimen Preparation**

The tricuspid valves from the right ventricle of fresh porcine hearts were used as specimens because of their high electrical conductivity.<sup>14</sup> Tissue samples (~6×3×1.5 cm) were clamped into a Plexiglas® frame to reduce random mechanical motion as shown in Fig. 3.1.

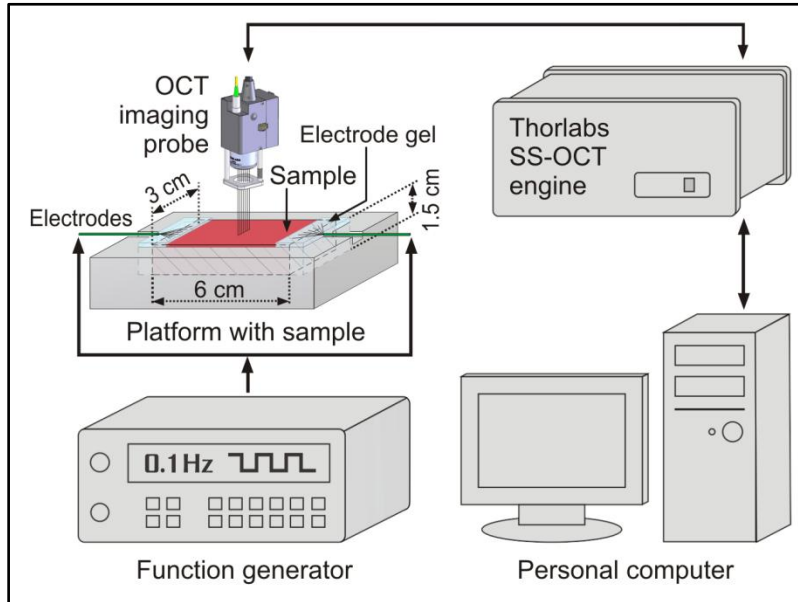


Figure 3.1 Schematic presentation of the experimental setup.

Electrodes made of 24 AWG PVC 7x32 tinned copper wire (Copper Industries Belden Division, Richmond, IN) were placed 6 cm apart on the opposite sides of the surface of the sample. Each electrode was covered with Spectra 360 electrically conductive gel (Parker Laboratories, Fairfield, NJ) to improve the electrical contact. A synthetic function generator (Stanford Research, CA, model DS335) was used as power source to generate square-wave electrical signals of 10 V amplitude and of 0.1 Hz frequency. A thin layer plastic membrane (Resinite packaging film, AEP Canada Inc.) was placed over top of the sample to reduce dehydration. Each specimen was left at room temperature for 5 hours before the experiment to reduce thermal artifacts.

### 3.2.2 OCT Instrumentation

A fiber based swept source OCT system (model #SL1325-P16, Thorlabs, NJ) employed a broadband light source with a central wavelength of 1310 nm and spectral bandwidth of 70 nm. The system's optical axial and transverse resolutions in air were 10.8  $\mu\text{m}$  and 25  $\mu\text{m}$ ,

respectively. The detector signal was digitized using a 16-bit 1.25 MHz data acquisition card (PCIe-6363, National Instruments) with a sampling speed of 50 MS/s. Thorlabs Swept-Source OCT Microscope software (version 2.3.0) running on a Windows XP personal computer (Intel, 3.6-GHz dual-core processor) managed data acquisition and image display. The data was collected in the form of 16-bit raw fringe data points (FRG format) which were processed to form 1024-pixel-wide×512-pixel-deep complex frames that were later used to calculate phase images. Imaging speed was one frame per second to assure adequate sampling. Consistent with the pixilation numbers above, each frame contained 1024 A-scans (lateral dimension = 3mm).

### **3.2.3 Experiment Protocol (Data Acquisition)**

Measurements with different cardiac tissue samples were performed to investigate the effects of a low-frequency electric field (0.1 Hz) on the backscattered signal phase changes in two-dimensional (B-mode) OCT phase images. A-scans were obtained with the probe scanning laterally along the middle of the sample (3cm from each electrode) with and without an applied electric field. The longest dimension of the sample was positioned perpendicular to the OCT probe. The B-mode OCT signals were organized in frames of 1024 consecutive A-scans (1024×512 pixels images) with axial scan rate of 16 kHz as shown in Fig. 3.2. Frames were acquired every second. Each experiment lasted for 480 seconds with the AC voltage application within the interval from 120s to 300s.

### **3.3 Development of phase imaging algorithm**

The approach to process the phase of OCT signals involved several steps [Figure 3.3].



After raw phase unwrapping (step 2), smoothing (step 3) and angular de-trending (step 4), for each  $(x,z)$  pixel of all phase images, the temporal profile  $P(t)$  [like in Figure 7(a)] of the corresponding OCT signal was extracted from the  $P(x,z,t)$  matrix. After that, the temporal de-trending procedure (step 6) was done to all 1024 x 512 temporal profiles  $P(t)$ . The portion of the signal during electric field application was extracted for further Fourier analysis (step 7) resulting in two (background and EIOC) phase images. Final image related to tissue electro-kinetic response was obtained after pixel-by-pixel division of EIOC image by the background image (last step). Each of the steps summarized in Figure 3.3 are briefly discussed below:

1. Raw phase calculation. The raw phase frames were calculated pixel-by-pixel from all the complex OCT signal frames using standard *angle* function in Matlab (Mathworks, Natick, MA).

2. Phase unwrapping. At this step, each A-line of each frame was unwrapped (*unwrap* function in Matlab). The typical resulting temporal profile of one A-line is shown in Figure 3.4(a). The periodic changes in optical signal phase between 120<sup>th</sup> and 300<sup>th</sup> seconds of the experiment reflect the periodic change of the polarity of external electric field in the same time interval (36 changes of polarity in 18 full cycles during 3 minutes of AC application). These oscillations are clearly seen because the field shifts the interstitial fluids periodically, which changes light scattering and absorbance by affecting the mutual alignment of collagen fibrils in tissue.<sup>15</sup>

3-4. Smoothing and angular de-trending. After forming a single axial profile from each frame containing 1024 A-lines, smoothing and angular de-trending were applied. The necessity of these steps rose from the fact that optical phase noise significantly affects the quality of resulting phase signals.

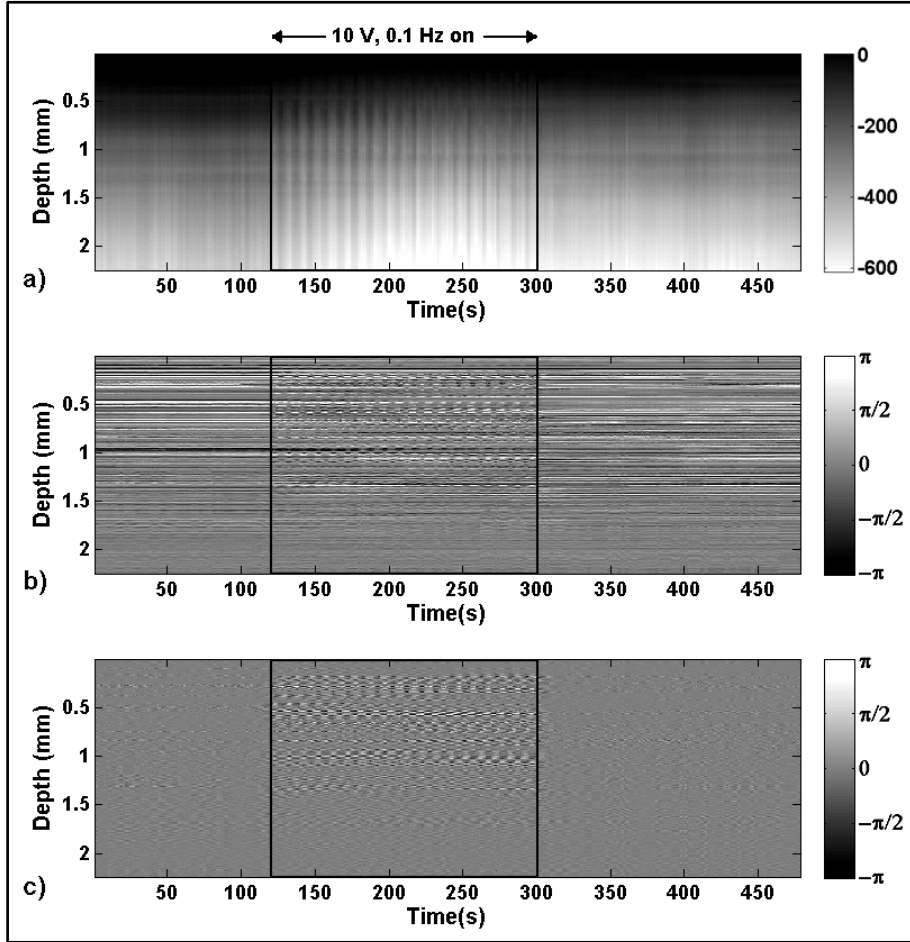


Figure 3.4 Typical phase temporal profiles for all depths of one A-line with grey scale bars in radians: (a) unwrapped phase (step 2 of the algorithm); (b) angular de-trended phase (step 4 of the algorithm); (c) temporal de-trended phase (step 6 of the algorithm).

Figure 3.5(a) illustrates the unwrapped phase before the application of electric field to the sample for one of the A-lines ( $t = 38s$ ). Ideally, before electric field application all unwrapped phases should be identical but significant fluctuations about the general trend caused by mechanical movements of the laterally scanning probe and vibrations of the experimental setup were noted [Figure 3.5(b)]. In order to eliminate this random fluctuation and obtain the real optical phase change, angular de-trending was implemented. Each A-line was unwrapped and

then smoothed (*smooth* function in Matlab) within the range of the nearest 5 points of the phase curve [Figure 3.5(a) inset].

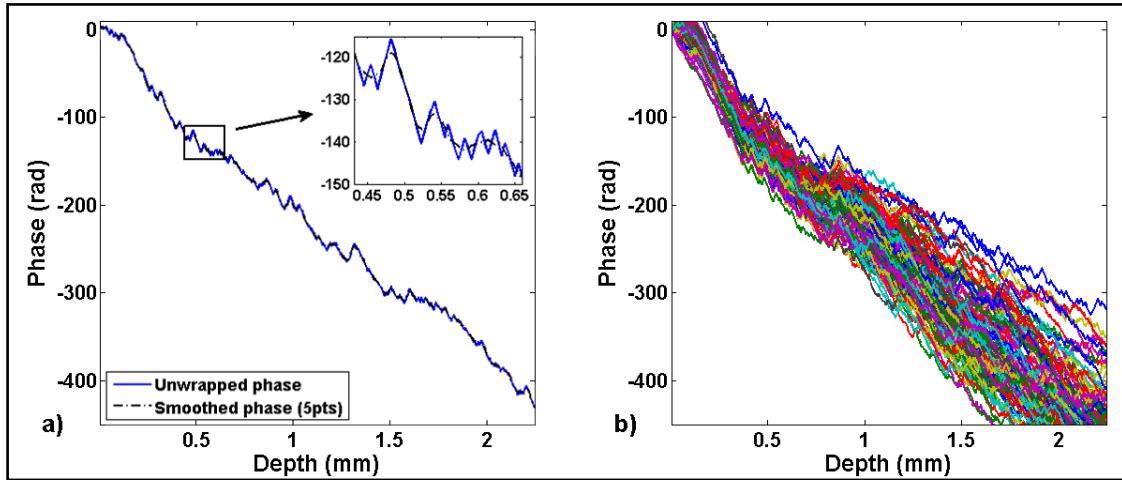


Figure 3.5 Unwrapped phase curves before application of electric field to the sample in B-mode: a) single line,  $t = 38$  s; b) all the lines,  $t = 1 - 110$  s.

After this step, the smoothed curve was subtracted from the original unwrapped curve to get the phase features. The range for smoothing (5 points) was selected such as not to exceed  $[-\pi \div \pi]$  range of the resulting angular de-trended phase. Figure 3.6 demonstrates how different smoothing ranges affect the resulting phase images in B-Mode if  $[-\pi \div \pi]$  angular de-trending range is exceeded. The three same unwrapped phase curves are shown at the top of the Figures 3.6 (a), (b) and (c) with corresponding B-mode phase images at the bottom that were obtained after averaging all angular de-trended phase frames from the time interval before electric field application. With linearly increasing number of points for smoothing of unwrapped phase curve, the noise level linearly dominates the signal causing the quality of the final image to decrease. For 21 nearest points smoothing [Fig. 3.6(b)], phase image loses its sharpness; for 45 points [Fig. 3.6(c)] it becomes so blurred that only contour of the sample can be distinguished.

The typical resulting temporal profile of one A-line after step 4 is shown in Figure 3.4(b).

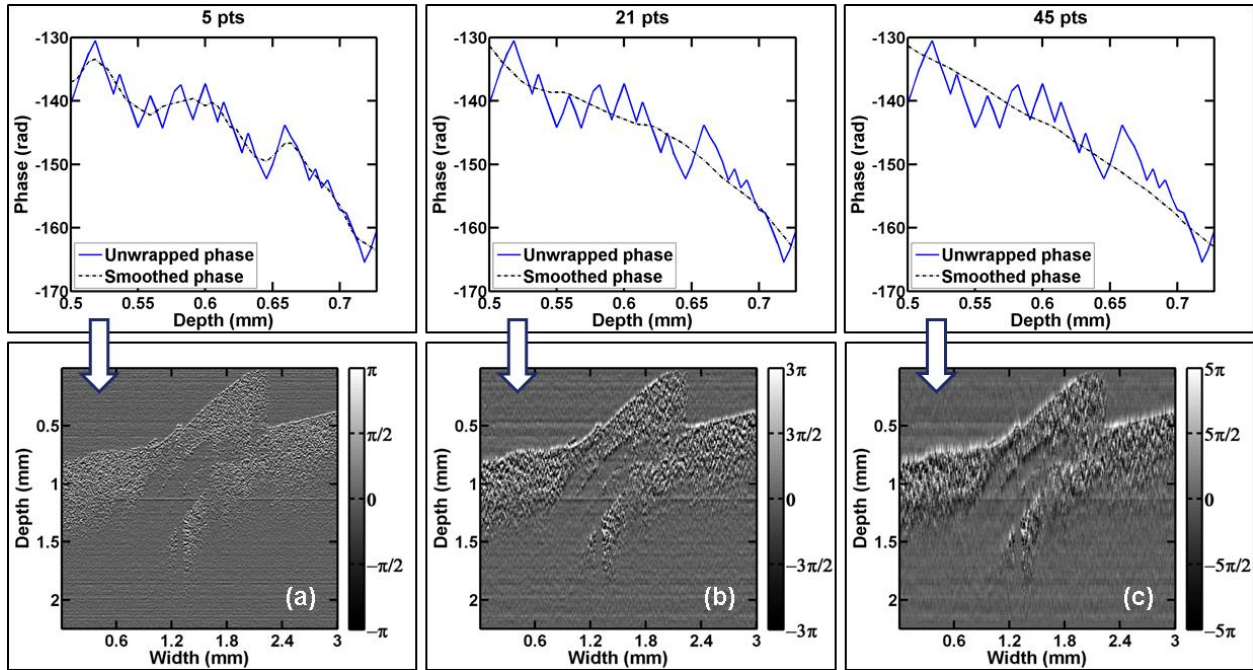


Figure 3.6 The different range for smoothing the phase curves in angular de-trending procedure and corresponding 2D phase images: (a) 5 nearest points; (b) 21 nearest points; (c) 45 nearest points. Phase images were obtained after averaging 110 angular de-trended phase frames before AC application. Gray bars on the right of each image indicate the resulting difference between unwrapped and smoothed curves in radians.

5. Normalization to the baseline. The OCT signal phase was then normalized to the baseline using mean averaging. For that the average of each A-line was calculated (*mean* function in Matlab) and then subtracted from each point value of this A-line. Figure 3.7(a) demonstrates the evolution of peak-to-peak phases of a typical transverse OCT signal (i.e. one depth pixel of one A-line of 2-D phase image) taken from 1.04 mm depth of a porcine heart sample and plotted as a function of time (480 seconds of the experiment). The phase of the OCT signal oscillates with the applied voltage. 18 oscillations within 180 second of 0.1Hz electric field application show the match of the external driving force and internal changes in tissue reflected by changes in backscattered optical signal phase.

6. Temporal de-trending. To eliminate the slow trend in the signal (which was reported<sup>16</sup> to be common for the SS-OCT sources) for further analysis, Savitzky-Golay algorithm<sup>17</sup> (*sgolay* in

Matlab) was used. The estimated trend was subtracted from the signal to obtain the de-trended signal. Figure 3.7(b) shows the peak-to-peak de-trended phase of the same transverse signal at 1.04 mm from the tissue surface before, during, and after the electric field application. The temporal de-trended profiles of one arbitrary A-line for all the depths are shown in Figure 3.4(c). The motivation for this de-trending procedure was the elimination of the spurious frequencies in the spectrum.

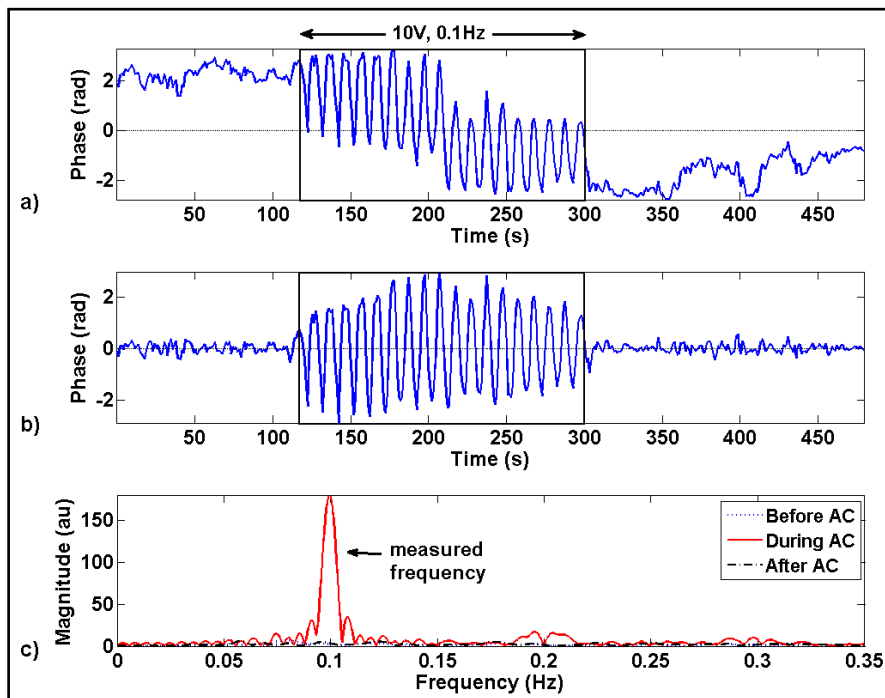


Figure 3.7 (a) The time course of a typical OCT signal phase before, during (inside the solid square), and after the AC application. (b) The de-trended signal. (c) FFT transforms of signal portions before, during and after AC application. Peak in the spectra marked “measured frequency” corresponds to the same frequency of the applied electric field (0.1 Hz).

7. Fourier analysis. The Fast Fourier Transform (FFT) algorithm (*fft* function in Matlab) on the portion of signal during electric field application was used to calculate the frequency and magnitude of OCT signal phase change [Figure 3.7(c)]. The main peak in the spectrum in figure 3.7(c) and its harmonics were related to the applied square waveform. In order to improve result

accuracy, a set of fast Fourier transforms was applied to the de-trended time profile to obtain a spectrum  $S_f(x,z)$  [Figure 3.3, step 7] instead of only one. For this purpose Matlab *pwelch* function was used. The signal was divided into 5 sections with 50% overlap; each section was windowed with a Hamming window (to reduce “spectral leakage”). Then FFTs for 5 modified periodograms were computed and averaged. A small window was chosen within the FFT spectrum at the expected frequency of the applied AC field (between  $0.959f_0$  and  $1.041f_0$ ). Lastly, the magnitude of the resulting  $S_f(x,z)$  spectrum at the frequency of the applied electric field ( $f_0 = 0.1$  Hz) was mapped to that  $(x,z)$  pixel to construct the OCT-based Electrically Induced Optical Changes (EIOC) image. The total processing time took 6 minutes on an AMD Bulldozer® 4.0 GHz 8-core system

### 3.4 Results

In order to verify the ability of the technique to image the electro-kinetic properties of tissue, a 1 mm diameter dielectric (i.e. electrically insulating) optical fiber was inserted into the middle of the sample at an arbitrary angle as shown in Figures 3.8(a) and (b), to represent a negative control (i.e., the averaged amplitude and phase images before AC application).

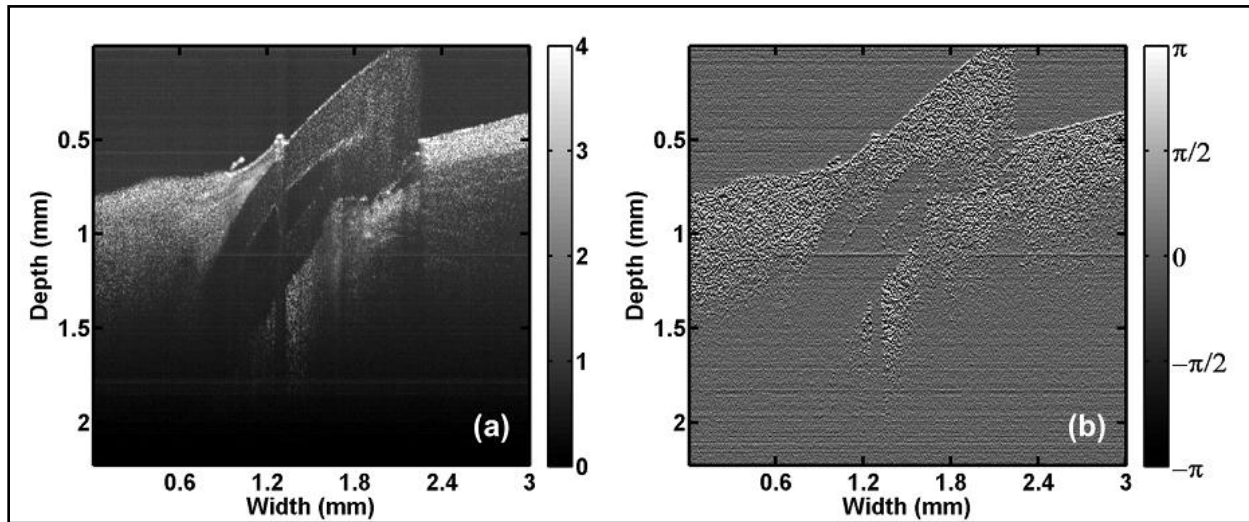


Figure 3.8 The averaged (110 frames) amplitude<sup>10</sup> (a) and phase (b) OCT images before AC application with gray bars in log scale for amplitude and radians for phase.

Then two sets of 2D phase images were calculated and shown in figures – averaged images [Figure 3.9] and electrically induced optical changes (EIOC) images [Figure 3.10] to clearly demonstrate the difference between them.

Averaged phase images before, during and after external electric field application (Figures 3.9(a), (b) and (c)) were obtained after the angular de-trending step of the algorithm. In order to eliminate phase background fluctuations, background images were computed by using standard deviation method (Figures 3.9(d), (e) and (f)). Averaged phase images were then normalized (divided) pixel-by-pixel by the background images (Figures 3.9(g), (h) and (i)).

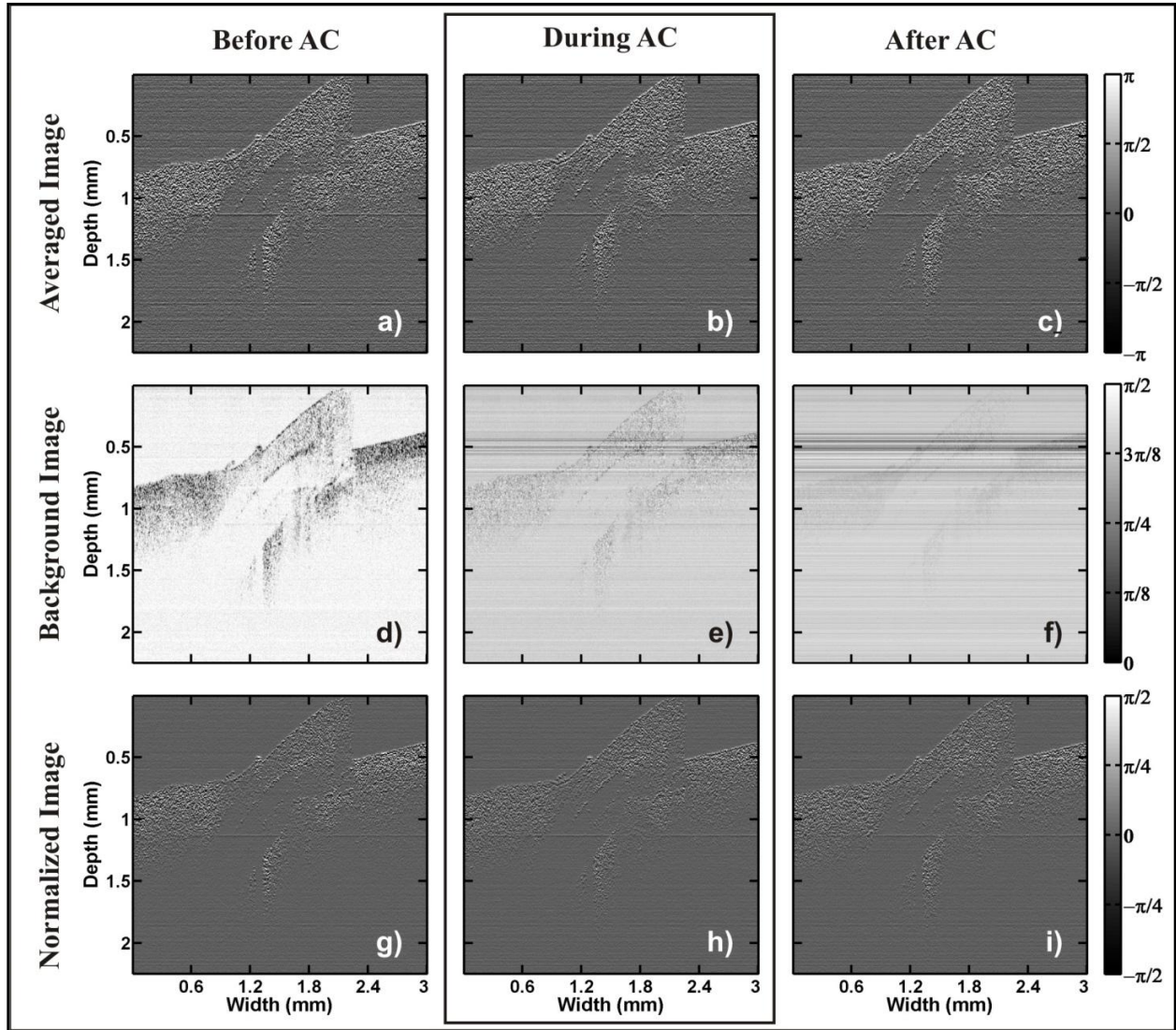


Figure 3.9 1<sup>st</sup> row: Averaged phase images before (a), during (b) and after (c) AC application; 2<sup>nd</sup> row: background phase images before (d), during (e) and after (f) AC application. 3<sup>rd</sup> row: normalized averaged phase images before (g), during (h) and after (i) AC application.

Figure 10 displays three sets of images before, during and after AC application. The resultant processed Electrically Induced Optical Changes (EIOC) phase image is shown in Fig 3.10(b). In the figure, the optical fiber cladding material surrounding the transparent core can clearly be distinguished.

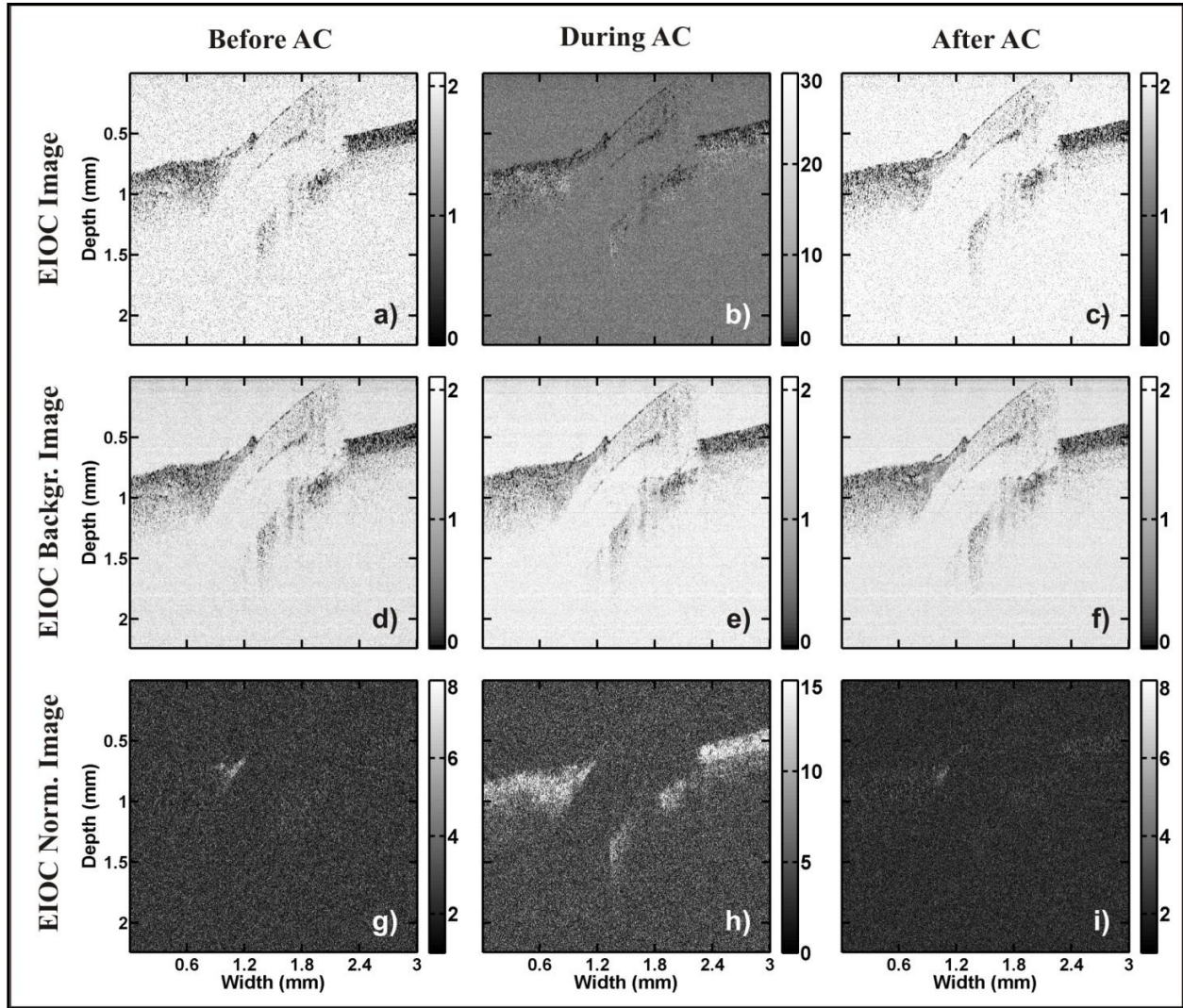


Figure 3.10 *1<sup>st</sup> row*: EIOC phase images before (a), during (b) and after (c) AC application; *2<sup>nd</sup> row*: background phase images before (d), during (e) and after (f) AC application. *3<sup>rd</sup> row*: normalized EIOC phase images before (g), during (h) and after (i) AC application. Note that before and after AC application the resulting images (g) and (i) carry no information due to absence of electric current in the sample while (h) clearly demonstrates the difference during AC application.

Although no electric current was induced inside the optical fiber inserted into the specimen, the fiber is visible in the EIOC phase image due to the background fluctuations giving rise to non-zero FFT values at  $f_0$ .

In order to eliminate the background fluctuations from the EIOC image, a background image [Figure 3.10(e)] was computed by using the FFT magnitude [example is shown in Figure 3.7(c)]

averaged over all frequencies except a small interval around  $f_0$  and the corresponding harmonics. Then the EIOC image was divided pixel-by-pixel by the background image. The result of this normalization is shown in Figure 3.10(h). One can clearly see that the fiber and a small piece of surface tissue to the left of the fiber in Figure 3.10(b) do not appear in Figure 3.10(h), in agreement with the absence of electric current in them. We thus conclude that the normalized EIOC image [Figure 3.10(h)] represents the information related to the electro-kinetic response of the sample.

For further verification of the method, the similar phase and background images were processed before and after electric field application [Figures 3.10(a), (d) and (f)]. As seen from the figures, the resulting images after normalization [Figures 3.10(g) and (i)] for both cases carry no information, which is in agreement with the absence of AC application to the sample.

### 3.4 Discussion

Obtained after OCT amplitude<sup>11</sup> and phase processing, both normalized EIOC images are shown in Figure 11 together with their cross-correlation image (*xcorr2* function in Matlab with 8x8 pixels grid). As one can see from the Figure 3.11 (a) and (b), the two images differ from each other except for some common features like tissue boundaries around optical fiber that was filtered out after normalization, and tissue sample surface. The inter-image cross-correlation analysis further emphasizes different information content by showing maximum cross-correlation value not exceeding 30%. This can be explained by the fact that amplitude and phase of OCT signals both depend on the backscattering property of tissues, but in different ways.

Assume we have a distribution of backscattering coefficient  $f(z)$  as a function of depth  $z$ . The measured spectrum  $I(\omega)$ , where  $\omega$  is positive, can be approximated as the positive frequency

components of the  $F(\omega)$ , the Fourier transform of  $f(z)$ .<sup>18</sup> When we reconstruct OCT images, we apply an inverse Fourier transform to  $I(\omega)$  to obtain  $g(z)$ . In normal OCT imaging, the amplitude of  $g(z)$  is displayed. Since  $I(\omega)$  are only positive frequency components of  $F(\omega)$ ,  $g(z) = \text{Hilbert}(f(z))$ , where  $\text{Hilbert}(f(z))$  means the complex Hilbert transform or the analytic signal of  $f(z)$ .<sup>19</sup> It is known that for a modulated signal, the amplitude of its complex Hilbert transform gives the envelope or the instantaneous amplitude of the signal, while the time rate of change of the instantaneous phase angle of its complex Hilbert transform gives the instantaneous frequency or the information on the oscillation under the envelope.<sup>20</sup> Therefore the phase of the OCT signals provides additional information on tissue properties, and phase images differ from amplitude images in our EIOC analysis and results.

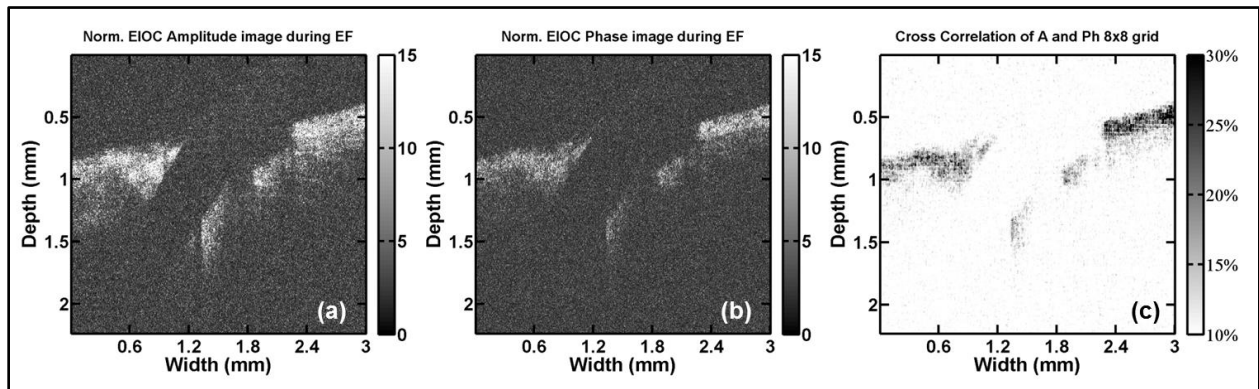


Figure 3.11 (a) normalized EIOC amplitude image<sup>11</sup>; (b) normalized EIOC phase image; (c) their cross-correlation image.

Yet even after all these procedures, the main questions of meaning and relevance of normalized EIOC phase image in Figure 3.11(b) remain. As was explained in step 4 of the proposed algorithm (angular de-trending procedure) we extracted local spatial phase variations from unwrapped phases. These variations were used to obtain phase images of the sample, representing therefore information about the local phase variation as a function of space. It is known that speckle pattern formation depends on the microscopic structure of the measured

object. Due to the application of the low frequency external electric field to the tissue, speckle patterns change their brightness and shape in resulting OCT images depending on the local EKP. The EIOC amplitude image therefore should represent the relative magnitude of electric field influence on biological tissue through changes of intensity of these speckle patterns. In addition to it, EIOC phase image should reflect the ratio of electric field influence on changes in speckle shapes. For better understanding of EIOC amplitude and phase images a further theoretical investigation is required.

In terms of information content, as for example was recently demonstrated,<sup>21</sup> EIOC information can assess the freshness of meat for quality control in food industry. Electro-kinetic responses of different tissues varies with meat freshness since variations of pH and permeability change with time due to the post-term glycolysis processes.<sup>15</sup>

In addition, our OCT phase measurements approach can be potentially used for identification and characterization of morphology and function of cancerous tissues. Today there exists a variety of advanced imaging modalities for this purpose, including OCT, but standard structural OCT imaging cannot detect early pathological changes in tissues.<sup>22</sup> One of the potential methods for early detection of pathology is through changes in electro-kinetic properties of tissue on the cellular level.<sup>23</sup> It was experimentally shown that malignant transformation of cells is correlated to the changes in the fixed charge density (FCD) on cell membranes. In another publication, it was reported that within the tumor, fixed charge density is significantly larger than the one on cell membranes within normal tissue at different pH levels.<sup>24</sup> Ultrasound has also showed a similar correlation of FCD in the extracellular matrix with physiological and pathological changes in tissue.<sup>25</sup> Dolowy<sup>26</sup> has demonstrated that cell membrane charge increases during tumorogenesis and decreases during necrosis. These previous

studies and our preliminary EIOC imaging results demonstrate a promising potential of developing a technique for monitoring the fixed charge density changes within tissues with amplitude and phase OCT analysis through their electro-kinetic responses.

### **3.4 Conclusion**

We have performed the sets of optical interferometric measurements with porcine heart tissue samples to investigate the effects of a low-frequency electric field on two-dimensional OCT phase images. The periodic changes in phase extracted from interference fringes during AC electric field application reflected the periodic change of the polarity of the field at the same frequency.

We developed the OCT signal phase processing method, demonstrating the capability to image the electro-kinetic response of biological tissues to the external electric field. The multi-step procedure of removing the background noise from the EIOC images was introduced. The ability of the method to image the electro-kinetic responses of tissues was demonstrated using an electrically non-responding material (1 mm diameter dielectric optical fiber) inserted into the tissue sample.

Normalized EIOC images obtained after OCT amplitude<sup>11</sup> and phase processing were found to differ from each other due to different kind of information on tissue properties contained in amplitude and phase data of OCT interference fringes. Further theoretical studies of the nature of the difference between the amplitude and phase EIOC images will follow up the experimental findings described in this paper.

### 3.4 Acknowledgements

This research was supported by NSERC Discovery grants (Y. Xu and V. Toronov), Canada Foundation of Innovation (V. X. D. Yang), and MITACS (B. Vuong and C. Sun).

### References

- [1] A. V. Delgado, F. González-Caballero, R. J. Hunter, L. K. Koopal, and J. Lyklema, "Measurement and interpretation of electrokinetic phenomena," *Journal of Colloid and Interface Science*, 309(2), 194-224 (2007).
  
- [2] J. Lyklema, *Fundamentals of Interface and Colloid Science* (Academic Press, 2005).
  
- [3] W.Y. Gu, W. M. Lai, V. C. Mow, "Transport of multi-electrolytes in charged hydrated biological soft tissues," *Porous Media: Theory and Experiments*, 34, 143-157 (1999).
  
- [4] C. Katnik and R. Waugh, "Electric fields induce reversible changes in the surface to volume ratio of micropipette-aspirated erythrocytes," *Biophysical Journal*, 57(4), 865-875 (1990).
  
- [5] S. Méthot, V. Moulin, D. Rancourt, M. Bourdages, D. Goulet, M. Plante, F. A. Auger, and L. Germain, "Morphological changes of human skin cells exposed to a DC electric field in vitro using a new exposure system," *Canadian Journal of Chemical Engineering*, 79(4), 668-677 (2001).
  
- [6] C. A. Erickson, and R. Nuccitelli, "Embryonic fibroblast motility and orientation can be influenced by physiological electric fields," *Journal of Cell Biology*, 98(1), 296-307 (1984).
  
- [7] O. Doganay and Y. Xu, "The effect of electric current in biological tissues on ultrasound echoes," *Proceedings of IEEE Ultrasonics Symposium*, 2103-06 (2009).

- [8] O. Doganay and Y. Xu, "Electric-field induced strain in biological tissues," *Journal of the Acoustical Society of America*, 128(5), EL261-EL267 (2010).
- [9] O. Doganay and Y. Xu, "Reversibility of electric-field induced mechanical changes (EIMC) in soft tissues," *IEEE. TUFFC-04263-2011.R1* (2012).
- [10] J. I. Youn, T. Akkin, and T. E. Milner, "Electrokinetic measurement of cartilage using differential phase optical coherence tomography," *Physiological Measurement*, 25(1), 85-95 (2004).
- [11] K. Wawrzyn, V. Demidov, B. Vuong, M. K. Harduar, C. Sun, V. X. D. Yang, O. Doganay, V. Toronov and Y. Xu, "Imaging the electro-kinetic response of biological tissues with optical coherence tomography," *Opt. Lett.* 38(14), 2572-2574 (2013).
- [12] J. G. Fujimoto, C. Pitris, S. A. Boppart, and M. E. Brezinski, "Optical coherence tomography: An emerging technology for biomedical imaging and optical biopsy," *Neoplasia* 2(1-2), 9-25 (2000).
- [13] S. R. Chinn, E. A. Swanson, J. G. Fujimoto, "OCT using a frequency-tunable optical source," *Opt. Lett.* 22(5), 340-342 (1997).
- [14] C. Gabriel, S. Gabriel and E. Corhout, "The dielectric properties of biological tissues: I. Literature survey," *Phys. Med. Biol.* 41 2231-49 (1996).
- [15] H. J. Swatland, "Basic Science for Carcass Grading," *VI Congresso Brasileiro de Cincia e Tecnologia de Carnes*, 6, 119 (2011).

- [16] D. C. Adler, R. Huber, and J. G. Fujimoto, "Phase-sensitive optical coherence tomography at up to 370,000 lines per second using buffered Fourier domain mode-locked lasers," *Optics Letters*, 32(6), 626-628 (2007).
- [17] A. Savitzky and M. J. E. Golay, "Smoothing and Differentiation of Data by Simplified Least Squares Procedures," *Analytical Chemistry* 36(8) (1964).
- [18] P. H. Tomlins and R. K. Wang, "Theory, developments and applications of optical coherence tomography," *J. Phys. D: Appl. Phys.* 38, 2519-2535 (2005).
- [19] E. C. Titchmarsh, "Introduction to the Theory of Fourier Integrals," Oxford: Clarendon (1937).
- [20] A. V. Oppenheim and R.W. Schaffer, "Discrete-Time Signal Processing," 2<sup>nd</sup> ed. Prentice-Hall (1998).
- [21] A. F. Pena, J. Devine, A. Doronin, I. Meglinski, "Imaging of interaction of low frequency electric fields with biological tissues by Optical Coherence Tomography," *Opt. Lett.* 38(14), 2629–2631 (2013).
- [22] A. F. Fercher, W. Drexler, C. K. Hitzenberger, and T. Lasser, "Optical coherence tomography - principles and applications," *Reports on Progress in Physics*, 66(2), 239-303 (2003).
- [23] B. Szachowicz-Petelska, I. Dobrzyska, Z. Figaszewski, and S. Sulkowski, "Changes in physico-chemical properties of human large intestine tumour cells membrane," *Molecular and Cellular Biochemistry*, 238(1-2), 41-47 (2002).

- [24] B. Szachowicz-Petelska, I. Dobrzynska, S. Sulkowski and Z. Figaszewski, "Characterization of the cell membrane during cancer transformation," *Journal of Environmental Biology*, 31(5), 845-850 (2010).
- [25] M. F. Insana, C.P. Barakat, M. Sridhar, K. K. Lindfors, "Viscoelastic imaging of breast tumor microenvironment with ultrasound," *Journal of Mammary Gland Biology and Neoplasia* 9(4), 393–404 (2004).
- [26] K. Dolowy, "Biochemistry of cell surface," *Progr. Surf. Sci.*, 15, 245-368 (1984).

## 4. SUMMARY OF RESULTS, CONCLUSIONS AND FUTURE WORK

### 4.1 Summary of results and conclusions

In this work we have developed two methods to obtain high-spatial-resolution information about the electro-kinetic response of biological tissues by combining optical coherence tomography (OCT) and low frequency external electric field.

In Chapter 2 we introduced the electrically induced optical changes (EIOC) imaging method. In this procedure, the goal was to image the electro-kinetic response of heart tissue by utilizing the amplitude of the OCT signal. It was demonstrated that the amplitude of the OCT signal increased with the amplitude and decreased with the frequency of the applied field. These results are consistent with those of the ultrasound imaging (after a frequency domain analysis of Fig. 5(a) and (c) in [1]) as well as with those of the differential phase reflectometry [2] for the cartilage surface displacements.

For the same level of applied electric field, it was found that the detected EIOC by OCT had a higher percentage of amplitude change than electrically induced mechanical changes (EIMC) by ultrasound. The most probable reason for this is that the wavelengths of light used in OCT (about 1  $\mu\text{m}$ ) are much smaller than the wavelengths of ultrasonic waves (150  $\mu\text{m}$  or greater), therefore OCT is more sensitive to the microscopic changes than the ultrasound. Since both ultrasound-detected EIMC and OCT-detected EIOC are reversible, they may have the same origin, probably due to the deformation of cells and extracellular matrix, and due to the electrically induced fluid flow as discussed in [3].

The developed two-dimensional image processing algorithm made it possible to visualize the electro-kinetic response of biological tissue being subjected to an external electric field. After filtering out background fluctuations giving rise to non-zero values in the frequency domain, the

2D EIOC image was demonstrated and compared with the structural OCT image. It was concluded that this image represented the information related to the local electro-kinetic properties of the tissue rather than the one translated from other locations on the light pathway.

In Chapter 3 we presented the second algorithm for imaging EKP in tissues based on phase information encoded in the OCT interferograms. The local spatial phase variations were extracted from complex OCT images to map EIOC in tissue samples by using Fourier transform method. These variations were used to obtain structural phase images of the sample, thus representing the information about the local phase variation as a function of space. This approach confirmed the robustness of the method because of identity of the results to those obtained after OCT signal amplitude analysis in Chapter 2: the periodic changes in phase during AC electric field application reflected the periodic change of the polarity of the field at the same frequency.

The developed phase processing technique allowed us to reconstruct the electro-kinetic response of biological tissues through EIOC phase images. Since the resulting phase signal was degraded by noise present in the fringe patterns, the multi-step procedure of removing the background noise from the EIOC images was introduced. The ability of the method to image the electro-kinetic responses of tissues was demonstrated using an electrically non-responding material (1 mm diameter dielectric optical fiber) inserted into the tissue sample.

Finally, the resulting EIOC amplitude and EIOC phase images were found to differ from each other except for some common features like tissue boundaries around optical fiber that was filtered out after normalization, and tissue sample surface. The inter-image cross-correlation analysis further emphasized different information content by showing maximum cross-correlation value not exceeding 30%. This was explained by the fact that amplitude and phase of OCT signals both depend on the backscattering property of tissues, but in different ways.

Limitations encountered in this study were related mainly to the sensitivity of the developed technique to experimental setup vibrations, although these effects were minimized by removing the background noise from the EIOC images in the frequency domain. In addition to signal processing, special air-floating optic table was used during the experiments to reduce setup vibrations.

Another limitation was the time-consuming signal processing. At the first stages of algorithm development it took several hours to reconstruct EIOC amplitude image on regular computer provided with standard OCT system. Algorithms required further optimizations and implementation of parallel computing techniques that eventually reduced the processing time to 6 minutes for both, EIOC amplitude and phase images on an AMD Bulldozer 4.0 GHz 8 core system in Matlab.

## **4.2 Future work**

The main challenge in Chapter 2 was to reduce detected signal noise during the experiments due to air circulation and building vibrations. In the future work additional procedures may be implemented into developed algorithm to increase the robustness of the method by filtering out the excessive noise. Partially this type of procedure was done in the second part of our study with phase estimation [Chapter 3], although the appropriate ranges of angular de-trending step are still questionable and require further investigations. In order to find out the appropriate solution, other methods discussed in Chapter 1.4 could be tested for amplitude/phase information extraction from detected interferograms. The most promising is a high-order ambiguity-function (HAF) based fringe analysis method that has been recently introduced [4] and demonstrated to provide accurate results with relatively less computational cost.

Both electro-kinetic response imaging methods were tested on limited number of porcine heart tissue samples. For future work it is essential to verify them on other tissues. Such experiments would make it possible to evaluate the consistency of the methods and to further compare EIOC amplitude and phase images.

Further theoretical studies of the nature of the difference between the EIOC amplitude and phase images are required to follow up the experimental findings described in this thesis. Thus, a 2-layer model of tissue influenced by electric field and probed by OCT may be implemented in the future work to derive the final expression of reconstructed interference field in the form of analytical signal [5]

$$A(z) = b(z)e^{-i\varphi(z)} + \eta(z),$$

Where  $b(z)$  represents the amplitude variations with depth  $z$ ,  $\varphi(z)$  – the interference phase to be estimated and  $\eta(z)$  – noise term inherited from the fringe pattern.

As this study was the first step in imaging the electro-kinetic response of biological tissues with OCT, a number of additional experiments is required in the future. Physiological changes in tissue (*in-vivo* and *ex-vivo*) reflect the changes in tissue electrical properties [6] and consequently may affect the resulting EIOC images. Experiments with such tissues may reveal certain regularities in EIOC images changes depending on tissue conditions. Besides, experiments on tissue-mimicking phantoms with known same optical but different electro-kinetic properties may potentially lead to better understanding of the information represented on EIOC images and development of the novel technique for monitoring the fixed charge density changes within the tissues. Such a technique being developed will provide more information than a set of usual OCT scans and will help in detecting early stage disease and therapy monitoring by OCT imaging.

## References

- [1] O. Doganay and Y. Xu, "Electric-field induced strain in biological tissues," *Journal of the Acoustical Society of America*, 128(5), EL261-EL267 (2010).
- [2] J. I. Youn, T. Akkin, and T. E. Milner, "Electrokinetic measurement of cartilage using differential phase optical coherence tomography," *Physiological Measurement*, 25(1), 85-95 (2004)
- [3] O. Doganay and Y. Xu, "Reversibility of electric-field induced mechanical changes (EIMC) in soft tissues," *IEEE. TUFFC-04263-2011.R1* (2012, in press).
- [4] S. S. Gorthi and P. Rastogi, "Numerical analysis of fringe patterns recorded in holographic interferometry using high-order ambiguity function," *J. Mod. Opt.*, 56 (8), 949-954 (2009).
- [5] D. Gabor, "Theory of communication," *J. Inst. Elec. Eng. (London)* 93III, 429–457 (1946).
- [6] E. Pacelat, R. Magjarevic, and V. Isgum, "Measurement of electrode-tissue interface characteristics during high current transcranial pulse electrical stimulation," *Measurement* 27, 133–143 (2000).